Astronomy & Astrophysics

The diversity of methanol maser morphologies from VLBI observations⋆

A. Bartkiewicz[1], M. Szymczak[1], H. J. van Langevelde[2,3], A. M. S. Richards[4], and Y. M. Pihlström[5,6]

[1] Toruń Centre for Astronomy, Nicolaus Copernicus University, Gagarina 11, 87-100 Toruń, Poland
e-mail: [annan;msz]@astro.uni.torun.pl
[2] Joint Institute for VLBI in Europe, Postbus 2, 7990 AA Dwingeloo, The Netherlands
e-mail: langevelde@jive.nl
[3] Sterrewacht Leiden, Postbus 9513, 2300 RA Leiden, The Netherlands
[4] Jodrell Bank Centre for Astrophysics, School of Physics and Astronomy, University of Manchester, M13 9PL, UK
e-mail: a.m.s.richards@manchester.ac.uk
[5] Department of Physics and Astronomy, MSC07 4220, University of New Mexico, Albuquerque, NM 87131, USA
e-mail: ylva@unm.edu
[6] National Radio Astronomy Observatory, 1003 Lopezville Road, Socorro, NM 87801, USA

ABSTRACT

Context. The 6.7 GHz methanol maser marks an early stage of high-mass star formation, but the origin of this maser is currently a matter of debate. In particular it is unclear whether the maser emission arises in discs, outflows or behind shocks running into rotating molecular clouds.
Aims. We investigated which structures the methanol masers trace in the environment of high-mass protostar candidates by observing a homogenous sample of methanol masers selected from Torun surveys. We also probed their origins by looking for associated H II regions and IR emission.
Methods. We selected 30 methanol sources with improved position accuracies achieved using MERLIN and another 3 from the literature. We imaged 31 of these using the European VLBI Network's expanded array of telescopes with 5-cm (6-GHz) receivers. We used the VLA to search for 8.4 GHz radio continuum counterparts and inspected *Spitzer* GLIMPSE data at 3.6–8 μm from the archive.
Results. High angular resolution images allowed us to analyze the morphology and kinematics of the methanol masers in great detail and verify their association with radio continuum and mid-infrared emission. A new class of "ring-like" methanol masers in star-forming regions appeared to be suprisingly common, 29% of the sample.
Conclusions. The new morphology strongly suggests that methanol masers originate in the disc or torus around a proto- or a young massive star. However, the maser kinematics indicate the strong influence of outflow or infall. This suggests that they form at the interface between the disc/torus and a flow. This is also strongly supported by *Spitzer* results because the majority of the masers coincide with 4.5 μm emission to within less than 1″. Only four masers are associated with the central parts of UC H II regions. This implies that 6.7 GHz methanol maser emission occurs before H II region observable at cm wavelengths is formed.

Key words. stars: formation – ISM: molecules – masers – instrumentation: high angular resolution

1. Introduction

Methanol masers are commonly assumed to be associated with the environments of high-mass protostars, which provide the conditions required for methanol first to form on grains and then to be sublimated off, and finally to excite the maser transitions (Dartois et al. 1999; Cragg et al. 2002). Methanol maser emission at 6668.519 MHz is one of the strongest and most widespread (Menten 1991) of the the first observable manifestations of a newly formed high-mass star. Emission towards the archetypical source W3(OH) is characterized with a brightness temperature of up to ~3×10^{12} K from a spot of intrinsic size of ~0″0014 (Menten et al. 1992). The gas environment of even distant (>5 kpc) high-mass stars can thus be probed on scales as small as ~5 AU when observed with milliarcsecond (mas) resolution using Very Long Baseline Interferometry (VLBI).

All major methanol targeted surveys of high angular resolution taken to date are summarized in Table 1. This indicates the diversity of the sample selections and observing parameters, which might have affected the data interpretation.

The first observations of the 6.7 GHz maser line at arcsec resolution, using the ATCA, concentrated on the brightest sources (Norris et al. 1993), followed by more extensive surveys (Phillips et al. 1998; Walsh et al. 1998). The relative positions of individual maser spots were determined with ~0″05 accuracy and the distribution of bright (>0.5 Jy beam^{-1}) maser spots was resolved for the majority of targets. Various morphological structures, such as simple, linear, curved, complex and double, were found. The linear sizes varied between 190 and 5600 AU. Norris et al. (1993) found that in 10 out of the 15 sources imaged the masers are located along lines or arcs of which five sources

---

⋆ Tables 1–3, 6 and Figs. 3, 6 are only available in electronic form at
http://www.aanda.org

show a clear velocity gradient along the line. They proposed that the linear structures with velocity gradients are produced by the masers residing in rotating discs seen edge-on. Phillips et al. (1998) increased the sample of masers studied with the ATCA to 45 objects, finding that 17 of them show morphologies and monotonic velocity gradients consistent with the circumstellar disc hypothesis. Assuming a Keplerian disc, the enclosed masses range from 1 to 75 $M_{\odot}$. In a sample of 97 sources Walsh et al. (1998) found 36 masers with some linear structure but this was clearly-defined for only 9 sources. Therefore, the Keplerian disc hypothesis accounts for only a small proportion of their sources; most maser sites do not exhibit a systematic velocity gradient. They suggested that the masers form rather behind shock fronts.

The methanol masers are often not associated with detectable continuum emission at centimeter wavelengths. Twenty-five of sources in the sample of Phillips et al. (1998) are associated with an ultra-compact H II (UC H II) region wherein the methanol masers are slightly offset from the peak continuum emission. They argued that the methanol sources without an H II region are possibly associated with less massive stars than those with coincident radio continuum emission. Walsh et al. (1998) also found that most of their maser sources are not associated with radio continuum brighter than ~1 mJy, implying that the phase of methanol maser occurs before an observable UC H II region is formed. This suggestion was confirmed for another sample of high-mass protostellar candidates (Beuther et al. 2002).

The detailed spatial structure of the methanol maser emission in these sources should provide further clues to their origin. To date, only a few observations at mas resolution have been published. Minier et al. (2000) observed 14 bright sources with the EVN. In 10 targets they found elongated structures with linear velocity gradients, which can be interpreted in terms of a circumstellar edge-on disc model. However, the estimates of central mass with this model for all but one source seemed to be far lower than expected for a high-mass star. Minier et al. (2000) suggested that this could be because the detectable masers delineate only part of the full diameters of the discs. They also proposed other models, such as accelerating outflows and shock fronts. Dodson et al. (2004) used the LBA to image five maser sites with linear morphologies at arcsecond resolutions. Their milliarcsecond resolution data were interpreted using a model of an externally generated planar shock propagating through a rotating dense molecular clump or star-forming core.

Van der Walt et al. (2007) argued that the model of Dodson et al. is inconsistent with the observed kinematic properties of the masers. They concluded that the observed rest frame distribution of maser velocities can be reproduced well with a simple Keplerian-like disc model. Source NGC 7538 IRS 1 is understood to be a good example of an edge-on Keplerian disc (Minier et al. 2000; Pestalozzi et al. 2004). However, high angular resolution mid-infrared (MIR) data were used to demonstrate that the outflow scenario is also plausible since the maser is not oriented perpendicular to the outflow as expected (De Buizer & Minier 2005). The kinematic and spatial distribution of the 12 GHz methanol masers in W3(OH) were successfully fitted by a model of a conical bipolar outflow (Moscadelli et al. 2002).

The initial methanol imaging surveys were mostly of relatively low (arcsec) resolution, whilst very long baseline interferometer (VLBI) studies probably missed fainter emission, such as from the edges or the far side of putative discs. For the first time, we have studied a large sample, detecting 31 sources at mas resolution and ~10 mJy sensitivity, with sufficient astrometric precision to complete robust identifications. This enables us to test the competing hypotheses for the origins of methanol

6.7 GHz maser emission, namely circumstellar discs, outflows, or propagating shock fronts. In this paper, we present EVN[1] observations of the methanol line and VLA observations of continuum emission for a homogeneous sample of the methanol masers discovered in the Torun untargeted survey (Szymczak et al. 2000, 2002). The preliminary results of methanol observations were partly published in Bartkiewicz et al. (2004, 2006, 2009). As part of this survey the discovery of a ring structure in G23.657−00.127 was reported by Bartkiewicz et al. (2005). Our observations have enabled us to detect a wide diversity of methanol maser geometries and demonstrate for the first time that in a large fraction of sources the distribution of the spots is ring-like.

2. Observations and data reduction

2.1. Sample selection

The sources were selected from two previous samples obtained using the Torun 32 m antenna: the blind survey of the 6.7 GHz methanol maser line (Szymczak et al. 2002) and the methanol survey of IRAS-selected objects (Szymczak et al. 2000). The untargeted flux-limited ($3\sigma_{rms} \simeq 1.6$ Jy) complete survey of the Galactic plane region $20° \leq l \leq 40°$ and $|b| \leq 0°.52$ enabled the detection of 100 sources of which 26 were new. The same field includes 22 sources discovered in the earlier survey of IRAS-selected objects. These 48 objects were chosen as a sample for detailed studies. We note that the mean single-dish methanol maser flux density of these 48 sources is 16 Jy, a factor of 2 lower than that of the rest sources in the original samples. This may have introduced a selection effect for masers that are more distant, have intrinsically weaker maser emission, or are less aligned with the line of sight.

Depending on the maser flux densities the source coordinates obtained using the 32 m dish are accurate to within $25–70''$. We undertook astrometric measurements using the first two MERLIN[2] antennas to be equipped with 6.7-GHz receivers (Mark II and Cambridge). These single baseline observations detected 30 of the 48 objects, providing positions with sub-arcsecond accuracy (see Sect. 2.2). We included three additional objects in the same region that had not been detected in the Torun surveys, for which accurate positions are reported in the literature. These are: G22.357+00.066 (Walsh et al. 1998), G25.411+00.105, and G32.992+00.034 (Beuther et al. 2002). The total sample selected for VLBI observations comprised 33 sources in the Galactic within the region defined by $21.4° \leq l \leq 39.1°$ and $−0.38° \leq b \leq 0.56°$ (Table 2).

2.2. MERLIN astrometry

The MERLIN observations at a rest frame frequency of 6668.519 MHz were carried out during observing runs between 2002 May and June and 2003 March and May. The typical on-source observing time was about 1 h for each target, and frequent observations of nearby phase reference sources and other calibrators were completed. Standard single-baseline data reduction procedures were applied (Diamond et al. 2003) using AIPS (the Astronomical Image Processing System). We searched for emission from each target in its vector-averaged spectrum by shifting the phase center from $−200''$ to $+200''$ in right ascension and from $−500''$ to $+500''$ in declination (at $1''$ intervals) to locate

---

[1] The European VLBI Network.

[2] The Multi-Element Radio Linked Interferometer Network.

the position giving the maximum intensity for the main maser feature. We simultaneously inspected the phase, which should be close to 0° at this position in the spectral channels containing the main feature. Finally, we produced a large (40″ × 40″) dirty map of the main feature for the channel of the highest spectral signal-to-noise ratio, centered on the estimated position. The brightest spot was then assumed to be as the maser position. A typical beam was $200 \times 20 \, \text{mas}^2$ at a position angle of 20°. Because of the very poor $uv-$coverage, we were unable to derive the maser structures.

Methanol maser emission was detected towards 30 of the 48 sources observed, giving absolute positions of sufficient accuracy for follow-up EVN observations. The MERLIN single-baseline astrometric accuracy was between 0″.3 and 1″ in most cases, depending on the source brightness. However, the absolute position uncertainty of sources at |Dec.| < 3°.5 increased to 5–10″. The mean differences between the coordinates obtained using a single dish and using the MERLIN single baseline were 30″ ± 6″ and 20″ ± 4″ in right ascension and declination, respectively. No emission was detected towards the remaining 18 sources above a sensitvity limit of 0.3 Jy (Table 3). The possible causes of non-detection are: variability, large errors in the single dish positions, interference (for a few targets), or extended emission, resolved out by the interferometer.

2.3. EVN observations

The EVN observations of 33 targets in the 6.7 GHz methanol maser line were carried out in seven observing runs between 2003 and 2007 (projects EN001, EN003, EB031, EB034). The observing parameters are summarized in Table 4 including the date, duration of each run, working antennas, cycle time between the maser and phase-calibrator, spectral resolution, typical synthesized beam size, and $1\sigma_{\text{rms}}$ noise level in a spectral channel.

Each observing run included scans of 3C 345, which was adopted as a bandpass, delay and rate calibrator. Five or six sources were, typically, observed in each run, selected to be within a few degrees of each other in projection on the sky and of similar maser emission velocities. A phase-referencing scheme was applied in which a nearby, sufficiently bright phase-calibrator for each session was selected from the VLBA list. Details are given in Table 2. We used a spectral bandwidth of 2 MHz yielding a velocity coverage of $\sim100 \, \text{km s}^{-1}$. In all sessions, the Mk V recording system was used with the exception of the first epoch when data were recorded on tapes (Mk IV system). The data were correlated with the Mk IV Data Processor operated by JIVE with 1024 spectral channels. In 4a and 4b runs only, when all nine antennas were operating, data were correlated with 512 spectral channels in two passes i.e., separately for LHC and RHC polarization, because of the correlator limitations. Left- and right-hand circular polarization data were averaged to increase the signal-to-noise ratio.

2.3.1. Calibration and imaging

The data calibration and reduction were carried out in AIPS, employing standard procedures for spectral line observations. First, the amplitude was calibrated using measured antenna gain curves and system temperatures. In the second step, the parallactic angle corrections were added. The Effelsberg antenna was used as a reference when calibrating the data from all sessions. The instrumental delays for calibrated using phase-calibrator and 3C 345 observations. The phase-calibrator

was mapped and a few iterations of self-calibration were completed, gradually shortening the time interval from 120 min to 1 min. Flux densities of 240, 202, 80, and 237 mJy were obtained for phase-calibrators J1825−0737, J1834−0301, J1856+0610, and J1907+0127, respectively. The maser data were corrected for the effects of the Earth's rotation and its motion within the Solar System and towards the LSR. After applying all corrections from the calibration sources, we compiled preliminary maps of the channel containing the brightest and most compact peak. We then used the clean components of that map, if possible, as the starting model for further rounds of self-calibration. In two cases, high quality images could only be obtained after the first round of self-calibration using a default model at the pointing position.

We searched for emission using large (2″×2″) maps over the entire band. We then created naturally-weighted 0.5″ × 0.5″ cleaned images to use in analyzing maser properties. The beam sizes for each data set are listed in Table 4. The pixel separation was 1 mas. The rms noise levels in line-free channels were typically between 4 and 10 mJy beam^{-1} depending on the run. The positions of all maser spots (above $5\sigma_{\text{rms}}$) in each individual channel map were determined by fitting two-dimensional Gaussian components. The formal fitting errors were, typically, 0.01–0.15 mas in right ascension and 0.02–0.5 mas in declination, depending on the source strength and structure.

The astrometric accuracy for the 29 sources with phase-referenced maps is limited by four factors. Firstly, the phase-reference source positions have an accuracy of <1.5 mas. Secondly, the antenna positions have an accuracy of ~1 cm, corresponding to an uncertainty of ~1 mas in RA and 2–3 mas in Dec. Thirdly, the separations between the targets and phase reference sources were ≲4°.5, which translate into a potential phase solution transfer error equivalent to 2 mas in RA and 4–5 mas in Dec. Fourthly, the position uncertainty due to noise is given by (beamsize)/(signal-to-noise ratio), which is ≪1 mas for all our reference features. This infers a total astrometric uncertainty of 3 mas in RA and 6 mas in Dec. For the remaining four sources, we were unable to improve on the original MERLIN positions.

2.4. VLA continuum observations

In order to investigate the presence, position, and distribution of radio continuum emission associated with the 6.7 GHz methanol maser emission, we used the VLA at 8.4 GHz in A configuration (the project AB1250). Data were taken on 2007 August 18 for 12 h in a standard VLA continuum mode towards 30 sources in the sample. We did not observe the three sources that had not been included in the Torun surveys. We used 3C 286 as a flux calibrator and two phase-calibrators, 18517+0355 and 18323−1035, from a standard VLA list. To increase signal-to-noise ratio, we employed the fast switching mode with a cycle time between the phase-calibrator and the target of 50 s+250 s. This sequence lasted for 20 min for each target.

The data reduction was carried out following to the standard recipies from AIPS Cookbook Appendix A (NRAO 2007). The amplitude and phases of 3C 286 were corrected using the default source model and 3C 286 was then used to find the phase-calibrator flux densities. The antenna gains were calibrated using the phase-calibrator data. Some bad points were flagged and finally the images were created with natural weighting. The $1\sigma_{\text{rms}}$ noise level in the maps was typically ~50 μJy beam^{-1} and the beam was 0″.35 × 0″.25.

Table 4. Details of EVN observations.

Observing run	Date	Duration (h)	Telescopes[*]	Cycle time (min)	Spectral channel separation (km s^{-1})	Synthesized beam($\alpha \times \delta$; PA) (mas $\times$ mas;°)	Rms noise per channel (mJy beam^{-1})
1	2003 Jun. 08	12	CmJbEfOn	6.00+4.00	0.09	6 × 16; −1	10
2	2004 Nov. 11	12	CmDaEfMcNtOnTrWb	3.75+1.75	0.09	6 × 16; +7	4
3a	2006 Feb. 22	10	CmJbEfHhMcNtOnWb	3.75+1.75	0.09	5 × 15;+31	10
3b	2006 Feb. 23	10	CmJbEfHhMcOnWb	3.75+1.75	0.09	6 × 14;+34	7
4a	2007 Jun. 13	10	CmJbEfHhMcNtOnTrWb	3.25+1.75	0.18	6 × 12;+20	4
4b	2007 Jun. 14	10	CmJbEfHhMcNtOnTrWb	3.25+1.75	0.18	6 × 11;+25	4
4c	2007 Jun. 15	10	CmJbEfMcNtOnTrWb	3.25+1.75	0.09	6 × 13;+35	6

[*] Cm-Cambridge, Da-Darnhall, Jb-Jodrell Bank, Ef-Effelsberg, Hh-Hartebeesthoek, Mc-Medicina, Nt-Noto, On-Onsala, Tr-Toruń, Wb-Westerbork.

Table 5. Results of EVN observations.

Source Gll.lll ± bb.bbb	Position (J2000) RA(h m s)	Position (J2000) Dec.(° ′ ″)	V_p (km s^{-1})	ΔV (km s^{-1})	S_p (Jy beam^{-1})	Area (mas × mas)	PA(°)	Class[**]	Δ_{MIR} (″)
G21.407−00.254	18 31 06.33794	−10 21 37.4108	89.0	3.00	2.76	138 × 39	−87	C	0.23
G22.335−00.155	18 32 29.40704	−09 29 29.6840	35.6	3.10	1.71	49 × 11	+16	L	0.67
G22.357+00.066	18 31 44.12055	−09 22 12.3129	79.7	9.20	10.54	330 × 174	−5	C	0.51
G23.207−00.377	18 34 55.21212	−08 49 14.8926	77.1	13.20	9.30	313 × 255	−69	R	0.56
G23.389+00.185	18 33 14.32477	−08 23 57.4723	75.4	6.00	21.55	205 × 134	+59	R	0.16
G23.657−00.127	18 34 51.56482	−08 18 21.3045	82.6	10.80	3.62	351 × 345	−82	R	0.50
G23.707−00.198	18 35 12.36600	−08 17 39.3577	79.2	23.30	6.06	130 × 110	−83	A	0.74
G23.966−00.109	18 35 22.21469	−08 01 22.4698	70.9	4.20	5.47	35 × 4	−45	L	0.19
G24.148−00.009	18 35 20.94266	−07 48 55.6745	17.8	1.40	3.60	28 × 3	−11	L	0.16
G24.541+00.312	18 34 55.72152	−07 19 06.6504	105.7	6.80	7.75	137 × 53	+78	A	0.45
G24.634−00.324	18 37 22.71271	−07 31 42.1439	35.4	13.40	3.03	73 × 21	−60	R	1.01
G25.411+00.105	18 37 16.92106	−06 38 30.5017	97.3	5.20	3.43	225 × 162	+79	R	0.64
G26.598−00.024	18 39 55.92567	−05 38 44.6424	24.2	3.30	3.04	361 × 152	−76	R	0.39
G27.221+00.136	18 40 30.54608	−05 01 05.3947	118.8	16.10	12.54	104 × 79	+6	C	0.89
G28.817+00.365	18 42 37.34797	−03 29 40.9216	90.7	5.20	3.14	115 × 28	+45	A/R	4.71
G30.318+00.070	18 46 25.02621	−02 17 40.7539	36.1	1.90	0.52	50 × 6	−50	L	0.87
G30.400−00.296	18 47 52.29976	−02 23 16.0539	98.5	6.70	2.77	199 × 97	+47	C/R	2.28
G31.047+00.356	18 46 43.85506	−01 30 54.1551	80.7	6.30	1.99	68 × 27	+72	R	1.73
G31.156+00.045[*]	18 48 02.347	−01 33 35.095							6.62
G31.581+00.077	18 48 41.94108	−01 10 02.5281	95.6	4.80	2.72	217 × 105	+79	A/R	4.23
G32.992+00.034	18 51 25.58288	+00 04 08.3330	91.8	5.20	6.21	115 × 68	−80	C	1.48
G33.641−00.228[*]	18 53 32.563	+00 31 39.180	58.8	5.30	28.3	167 × 61	+66	A	1.22
G33.980−00.019	18 53 25.01833	+00 55 25.9760	58.9	6.90	3.78	89 × 43	+82	R	0.95
G34.751−00.093	18 55 05.22296	+01 34 36.2612	52.7	3.10	1.95	49 × 11	−56	R	0.47
G35.793−00.175[*]	18 57 16.894	+02 27 57.910	60.7	2.80	9.70	10 × 2	+65	L	1.12
G36.115+00.552	18 55 16.79345	+03 05 05.4140	73.0	14.80	11.74	1201 × 297	−79	P	2.42
G36.705+00.096	18 57 59.12288	+03 24 06.1124	53.1	10.60	7.58	64 × 18	−16	C	0.32
G37.030−00.039	18 59 03.64233	+03 37 45.0861	78.6	0.70	0.69	2 × 1	−15	S	0.61
G37.479−00.105[*]	19 00 07.145	+03 59 53.350							1.73
G37.598+00.425	18 58 26.79772	+04 20 45.4570	85.8	4.50	3.91	94 × 28	+87	C	1.24
G38.038−00.300	19 01 50.46947	+04 24 18.9559	55.7	4.20	2.17	31 × 23	+10	C	0.28
G38.203−00.067	19 01 18.73235	+04 39 34.2938	79.6	6.00	0.83	182 × 58	−44	C	1.74
G39.100+00.491	19 00 58.04036	+05 42 43.9214	15.3	3.30	2.07	183 × 37	+52	C	0.82

[*] Coordinates derived from the single MERLIN baseline data.
[**] Class of morphology as described in Sect. 3.3: S – simple, L – linear, R – ring, C – complex, A – arched, P – pair.

3. Results

3.1. Maser emission

We successfully mapped a total of 31 out of 33 methanol masers observed with the EVN. We were unable to image G31.156+00.045 and G37.479−00.105 because of the weakness (<30 mJy) of the emission and to strong spike artefacts in the channels at the maser velocity, respectively. We were unable to improve on the MERLIN astrometry for G33.641−00.228 and G35.793−00.175 due to a problem with the EVN phase-referencing that appeared during the first observing run. We created fringe rate maps of the brightest channels of the targets

but still failed to determine the absolute position of these two sources. The target sources were near zero declination (from +0°.5 to +2°.5). Furthermore, because of the use of only four EVN telescopes, the $uv-$plane coverage was poor for N−S baselines. It is probable that these factors together with a too long phase-referencing cycle time precluded a proper phase calibration. The position of the third source, G36.115+00.552, observed in the first run, was easily ascertained during the 4c run when eight antennas were working and the cycle time between the maser and phase-calibrator was shorter.

The results are summarized in Table 5. The names of the maser sources correspond to the Galactic coordinates of the

brightest spot of each target. The absolute coordinates, the LSR velocity (V_p), and the intensity (S_p) are given for the brightest spot of each target. We also indicate the velocity range of emission ΔV. The area containing all maser emission from each source was parameterised by measuring the extent of the maser emission along the line given by a least squares fit to the maser spot distribution (major axis and position angle) and in the perpendicular direction (minor axis). The morphological class based on the relative positions of methanol maser spots and the angular separation Δ_{MIR} of the brightest spot of each source from the nearest 4.5 μm source (see Sect. 4.2) are also given in Table 5.

In Fig. 1, we present the spectra and distribution of the methanol maser emission for the 31 imaged targets. The spectra were extracted from the map datacubes using the AIPS task ISPEC. They represent the total amount of emission seen in the maps. In order to display the detailed structures of masers, we show all the spots detected in each of the individual channel maps. If spots appear at the same positions within half of the beamwidth in at least three or two consecutive channels, for observations with a spectral resolution of 0.09 km s^{-1} and 0.18 km s^{-1}, respectively, we refer to them as a *cluster*. The relevant parameters of all maser clusters for each source are listed in Table 6: the position (ΔRA, ΔDec.) relative to the brightest spot (given in Table 5), the peak intensity (S_p), and the LSR velocity (V_{LSR}) of the brightest spot within a cluster. The velocity full-width at half-maximum (*FWHM*) and the fitted peak amplitude (S_{amp}) are given if the spectrum of the cluster has a Gaussian profile.

3.2. Radio continuum emission

We detected 8.4 GHz continuum emission in eight of the fields centered on methanol masers. Table 7 lists the continuum source names (derived from the Galactic coordinates of the 8.4-GHz peak fluxes), the peak and the integrated intensities, and the angular size of the radio continuum emission at the $3\sigma_{rms}$ level. We also provide the name of the nearest maser from the sample and the angular separation between the continuum peak and the brightest spot of the nearest methanol maser.

The contour maps of all detections are shown in Figs. 2 and 3. The majority of sources are single peaked and their angular sizes range from 0″.6 to 3″.8. Both G24.148−00.009 and G36.115+00.552 have integrated flux densities that are equivalent to their peak flux densities within the noise, suggesting that these sources are unresolved. The values given for these sources in Table 7 correspond to the angular size upper limits. G31.582+00.075 is one of the weakest sources (S_p = 0.43 mJy beam^{-1}) but has an exceptionally complex structure. It is extended (4″ × 3″) and contains multiple emission peaks. The typical upper limit ($3\sigma_{rms}$) for the fluxes of the remaining 22, non-detected sources is 0.15 mJy beam^{-1}.

The 6.7-GHz methanol maser emission is found to be within 0″.2 of the 8.4-GHz continuum position peaks of G24.148−00.009, G28.817+00.365, and G36.115+00.552. The maser spots of source G26.598−00.024 are 0″.8 from the NE edge of the radio continuum source. Therefore, these four sources are closely associated with the methanol masers (Fig. 2). The continuum object G31.160+00.045 is located 11″.9 from the nominal position of the maser source G31.156+00.045, but this maser has a position uncertainty of 10″ because we were unable to image it with the EVN (Sect. 3.1), so it may also be associated with the radio continuum. On the other hand, the continuum

source G31.582+00.075 has a separation of ~9″ from the maser G31.581+00.077, but the latter has a position accuracy of a few mas implying that the source and maser are unlikely to be associated.

We conclude that only 4 (possibly 5) of 30 masers are associated with radio continuum at 8.4 GHz. This is consistent with previous findings (Phillips et al. 1998; Walsh et al. 1998; Beuther et al. 2002) that the 6.7 GHz methanol masers are rarely associated with centimeter wavelength continuum emission. However, 24-GHz ATCA observations detected continuum emission associated with methanol masers toward which no continuum at 8.4 GHz had been previously detected (Longmore et al. 2007). This opens the possibility of methanol masers being associated with hyper-compact H II regions (HC H II), which are ptically thick at frequencies <10 GHz.

3.3. General properties of the 6.7 GHz methanol masers

In 31 sources, we detected a total of 1934 maser spots that form 333 clusters. The spectral profiles of 265 (80%) clusters are well fitted with a Gaussian. The mean *FWHM* is 0.41 ± 0.01 km s^{-1} and the median value is 0.37 km s^{-1}. This is consistent with results from single dish spectra at ~0.05 km s^{-1} resolution (Menten 1991; Caswell et al. 1995). Nineteen sources have complex spectra, that is indicative of spectral blending, so that the line width of individual features cannot be properly determined solely from the spectrum.

We compared the basic parameters of the spectra and distributions of all masers from the sample. However, we did not find any relationships between the line parameters such as *FWHM*, brightness temperature, velocity range of the maser emission, and the size and geometry of the maser region.

The sources show a wide diversity of structures. The following types of morphology can be identified (Table 5):

Simple – the emission appears in a narrow velocity range ($\Delta V = 0.7$ km s^{-1}) as a single peaked spectrum. The maser spots form one cluster of size smaller than a few mas. G37.030−00.039 is the only source with these properties. Its spectrum is obviously blended.

Linear – the maser spots form a line in the plane of the sky. The angular extent of these maser structures ranges from 9 to 54 mas. In some sources (G30.318+00.070, G35.793−00.175) a monotonic velocity gradient is clearly seen. There are five linear sources in the sample.

Ring – this morphology appears to be ubiquitous in our sample. The distributions of no less than nine sources display a ring structure. Using the GNU Octave script developed by Fitzgibbon et al. (1999), we fitted an ellipse to the spatial positions of the maser spots for each source. The results are summarized in Table 8. The semi-major (a) and semi-minor (b) axes range from 27 to 192 mas and from 15 to 128 mas, respectively. The average size of the semi-major axis and the standard dispersion in the mean is 89 ± 20 mas. The eccentricity (e) of the best-fit model ellipses ranges from 0.38 to 0.94. The average eccentricity and the standard dispersion of the mean is 0.79 ± 0.06. The emission spans a modest velocity range of (3.1−13.4 km s^{-1}). All nine sources possess MIR counterparts that coincide with the ellipse center to within less than 2″.5 (Table 5). In these objects it is very likely that ring-like maser emission surrounds a central embedded star (see Sect. 4.2). Three other sources (G28.817+00.365, G30.400−00.296, G31.581+00.077) have a ring-like morphology, although the separation between the MIR candidate counterpart and the ellipse center is greater than 2″.5 (Table 5). This is probably caused by the larger uncertainties in the maser
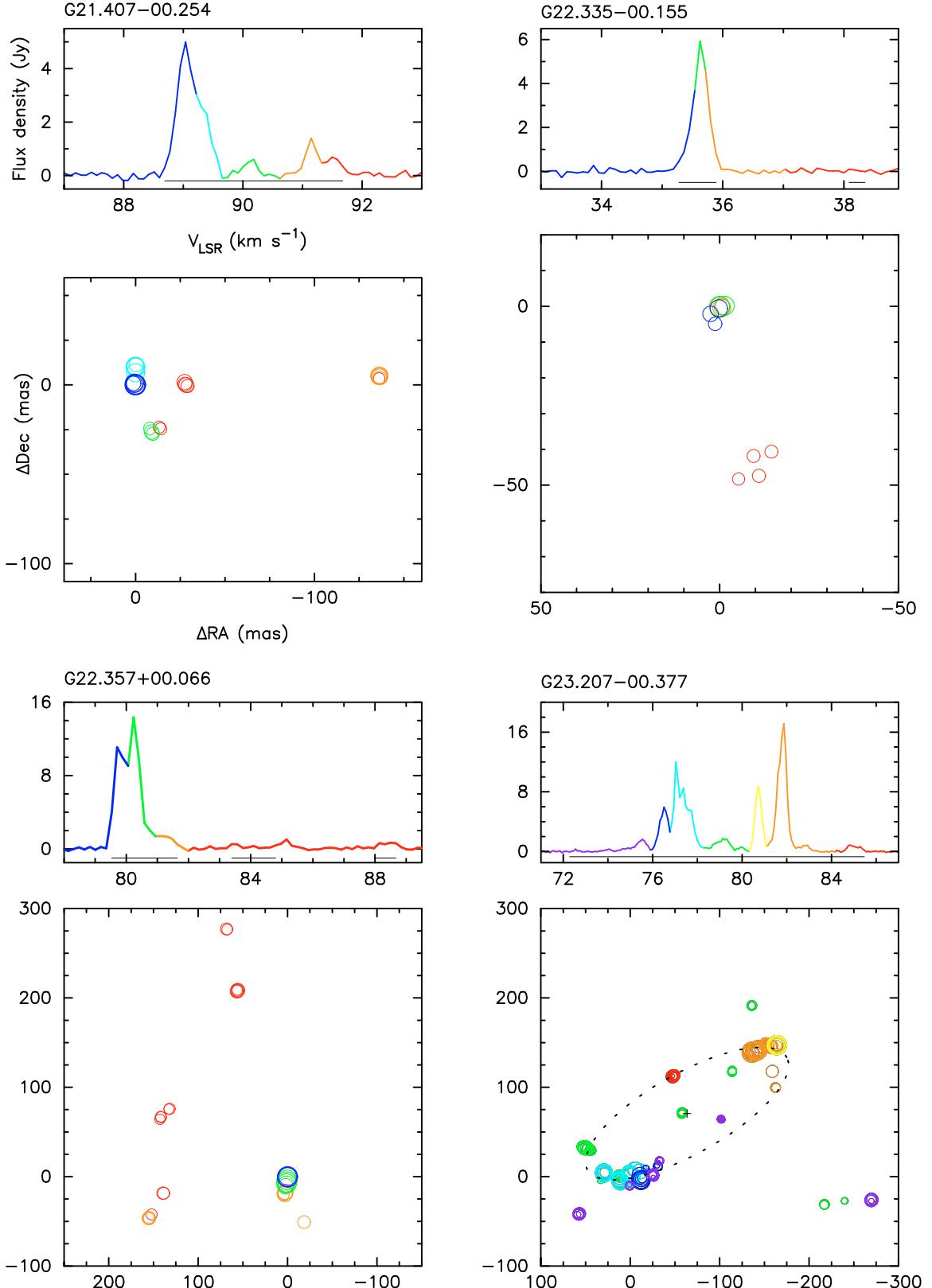
Fig. 1. Spectra and maps of 6.7 GHz methanol maser emission of sources detected with the EVN. The names are the Galactic coordinates of the brightest spot as listed in Table 5. The thin bars under the spectra show the velocity ranges of spots displayed. The coordinates are relative to the brightest spots (Table 5). The sizes of circles are proportional to the logarithm of the intensities of maser spots. The colors of circles relate to the LSR velocities as indicated in the spectra, respectively. For the sources with ring-like morphologies, the best-fit ellipse and its center are marked by a dotted curve and a cross, respectively. The crosses coincide (within the uncertainties) with *Spitzer* IRAC MIR emission (Sect. 4.2).

G23.389+00.185

G23.657−00.127

G23.707−00.198

G23.966−00.109
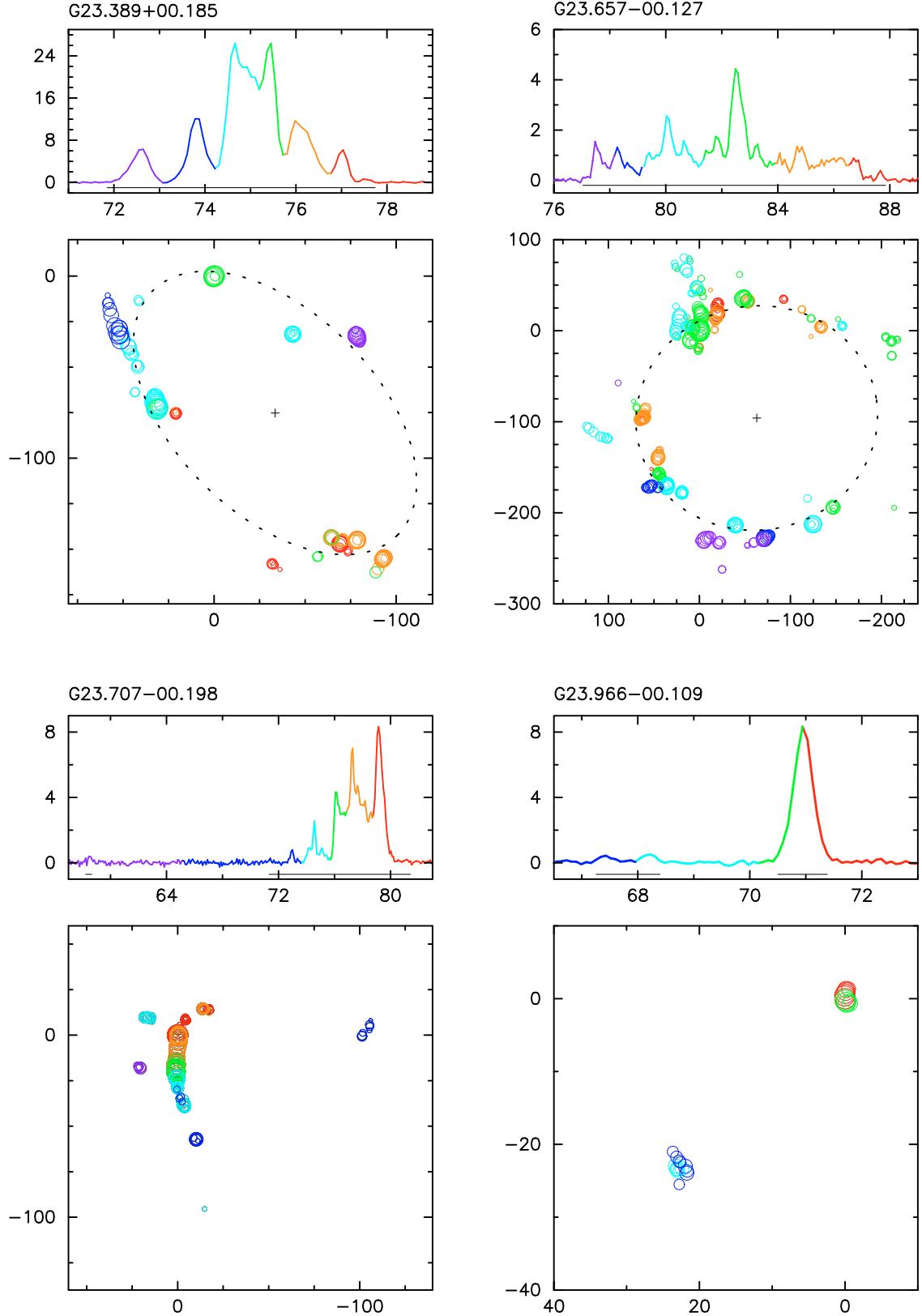
Fig. 1. continued.

positions, since all three sources are at declinations near 0°. These are assigned a tentative classification of the ring-like class in Table 5.

Arched – maser spots are distributed along an arc of between 70 and 220 mas in length. The entire structure may show a systematic velocity gradient. Three (or possibly five) sources exhibit this morphology.
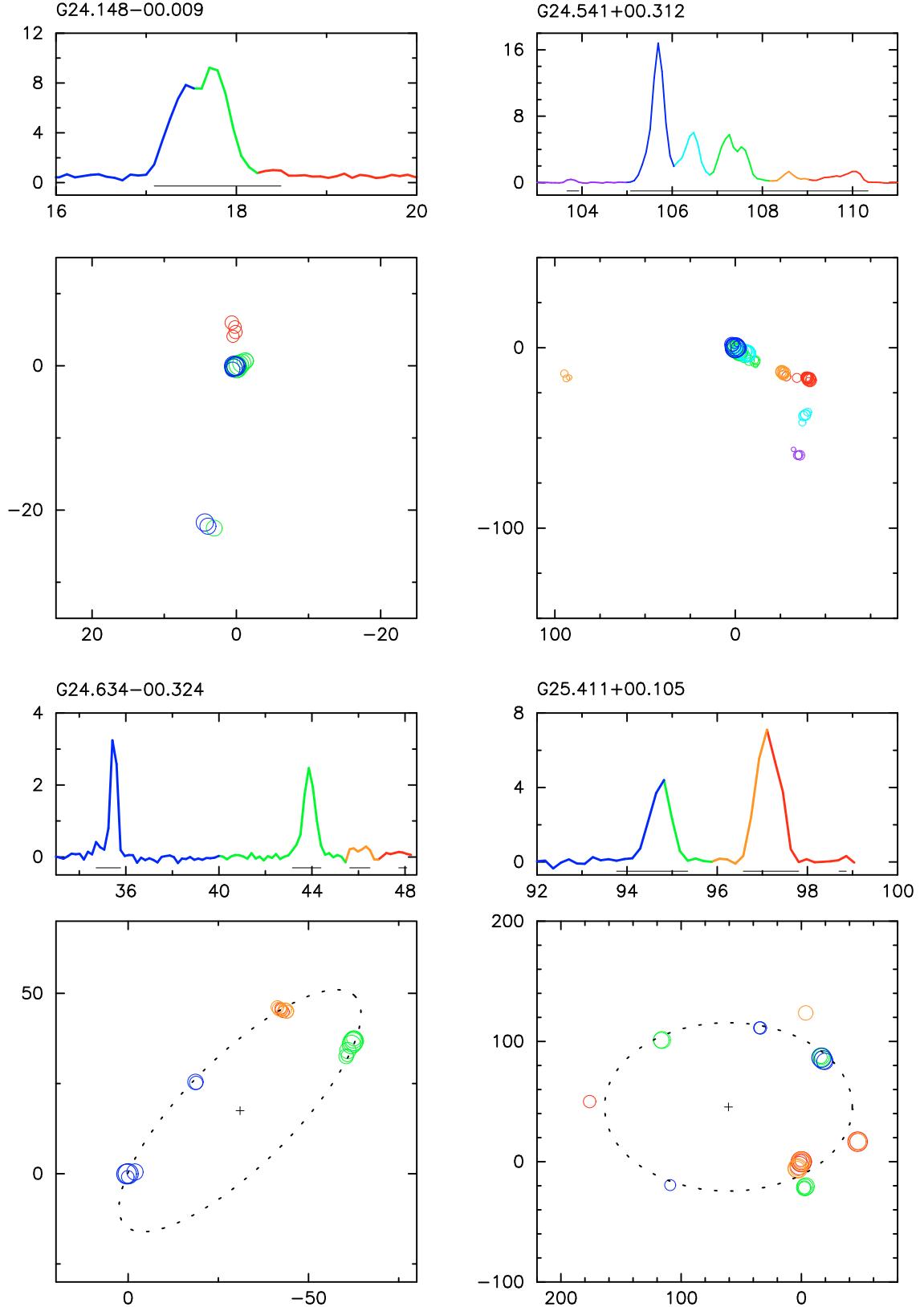
Fig. 1. continued.

Complex – 9 (possibly 10) sources, i.e. about one third of the sample, do not show any regularities in their spatial and velocity distributions. These sources vary greatly in size from 31×23 mas^2 to 330×174 mas^2.

Pair – this class was defined by Phillips et al. (1998), comprising two maser groups separated by ~1 arcsec with ≥ 10 km s^{-1} difference in velocity. The major axes of individual clusters are perpendicular to the line joining them. In our sample, we found only one source with such a morphology.
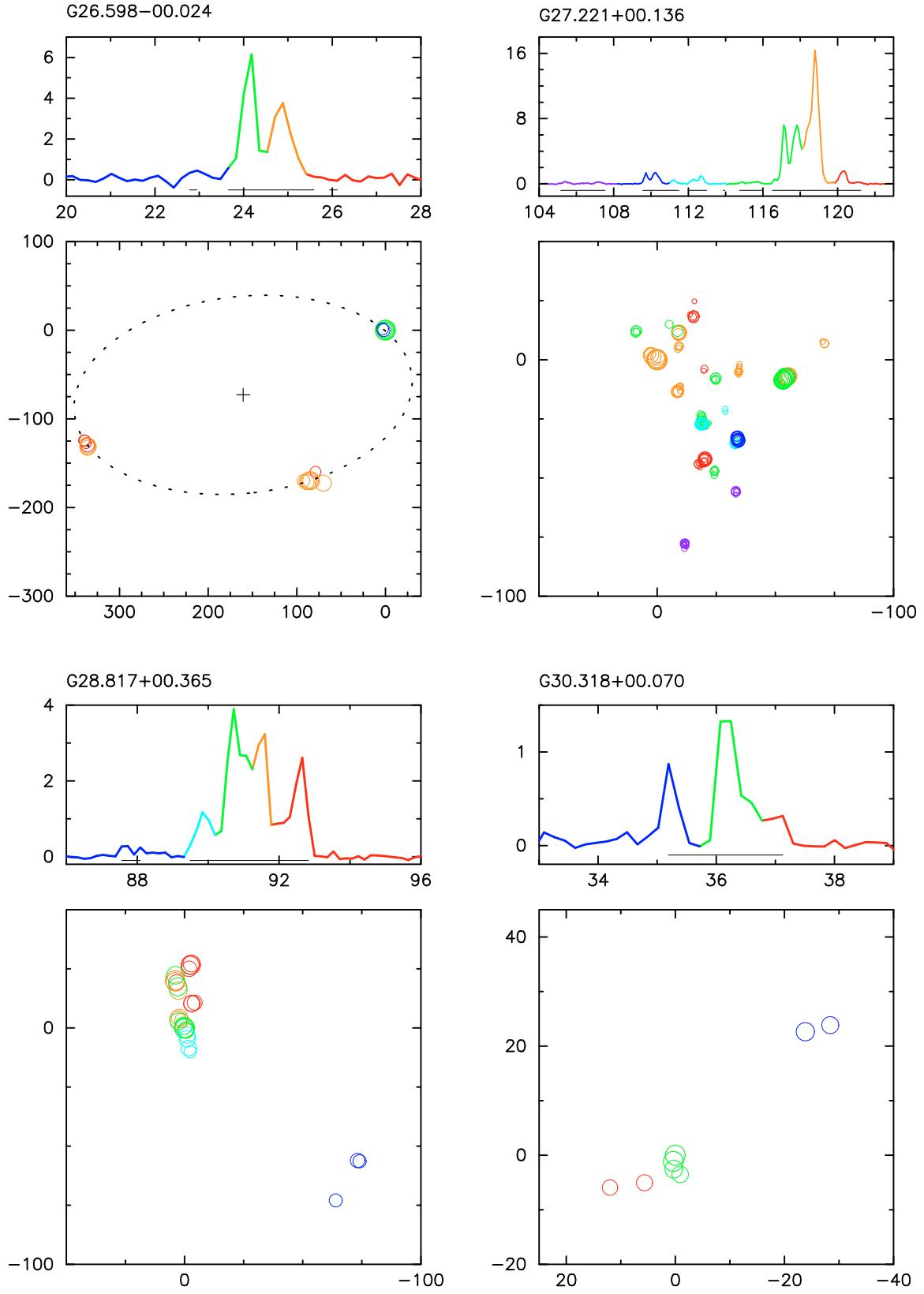
Fig. 1. continued.

The most striking aspect of this study is that we find that the commonest morphology of sources with a systematic maser structure is a ring-like distribution of emission, seen in ~29% of objects. These rings probably surround young massive objects (see Sect. 4). A similar proportion (~29–32%) of sources possess a complex morphology. Linear sources with a monotonic velocity gradient are relatively rare in the sample (~16%).

G30.400−00.296

G31.047+00.356

G31.581+00.077

G32.992+00.034
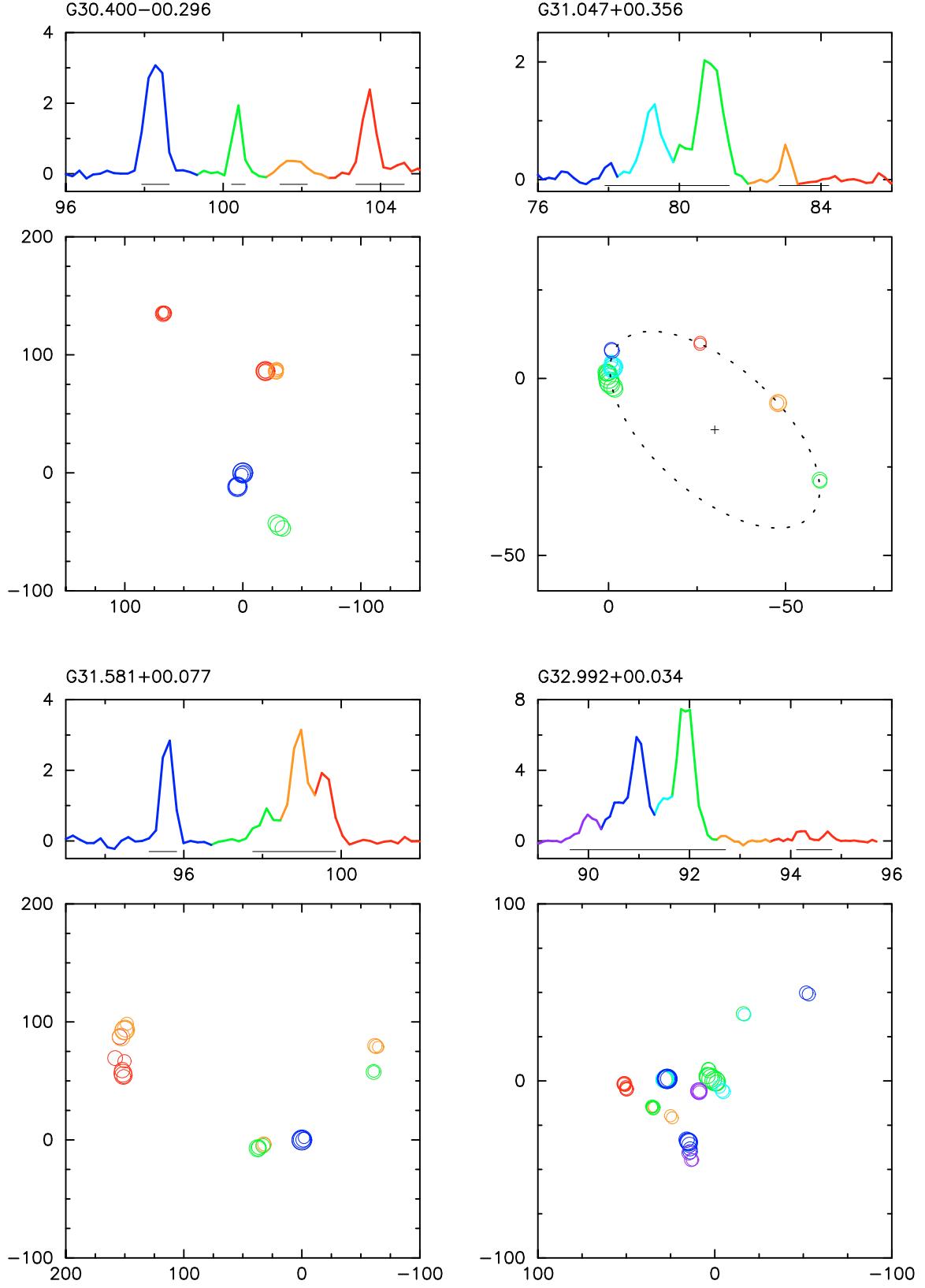
Fig. 1. continued.

3.4. Individual sources

This section presents comments on individual sources, including additional observational data relevant to the main aims of this paper. If not stated otherwise, we present the linear sizes of masers derived using the near (and far) kinematic distances given in Szymczak et al. (2005).

G22.357+00.066. The ATCA observations detected three maser spots (Walsh et al. 1998), while the EVN revealed 31 spots in 10 clusters. The strongest emission detected with both
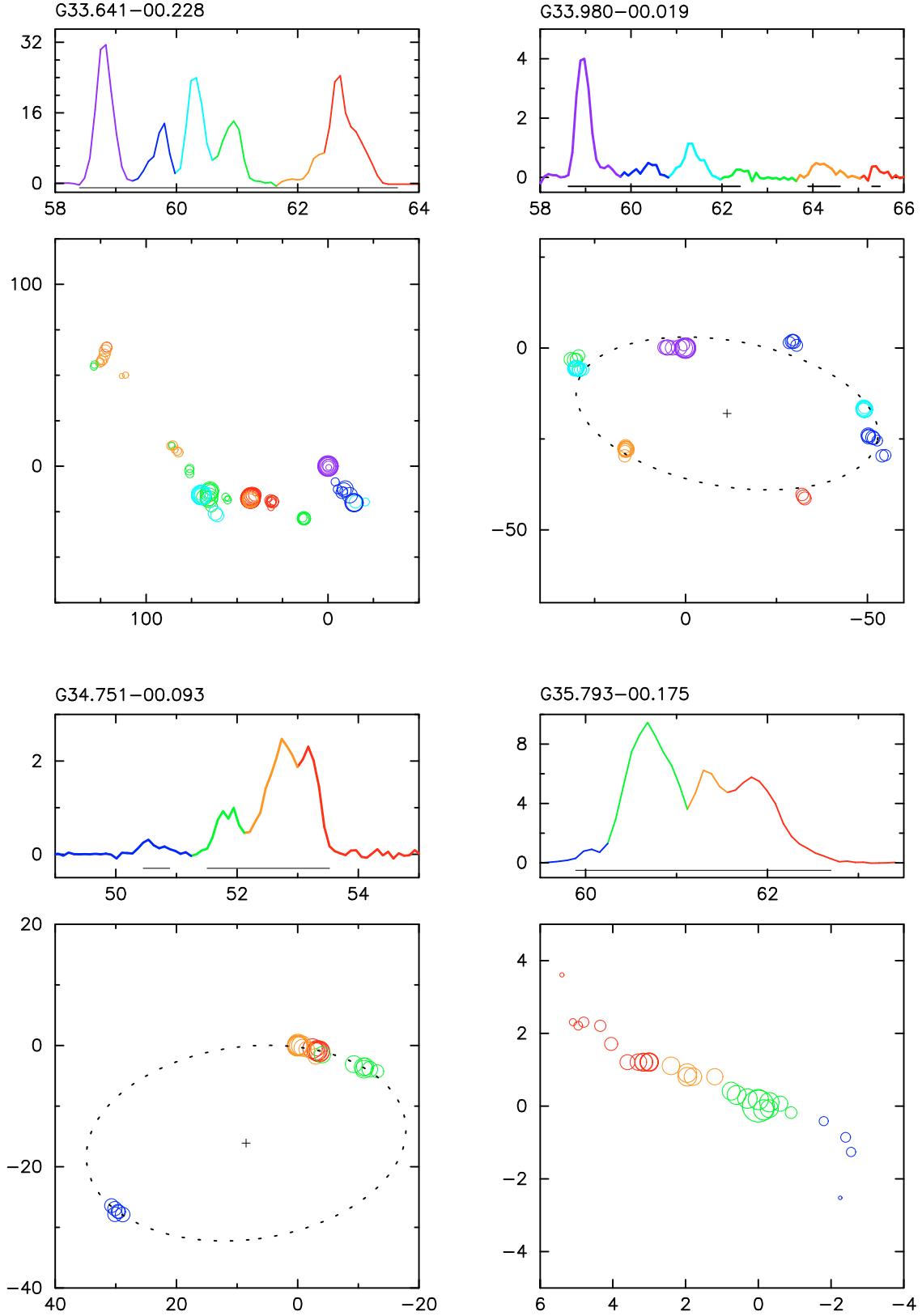
Fig. 1. continued.

interferometers, at $80.0\,\mathrm{km\,s^{-1}}$, coincides to within $1''.7$. We detected new emission at close to $88.5\,\mathrm{km\,s^{-1}}$, $0''.20$–$0''.27$ north of the brightest spot, but a $77.0\,\mathrm{km\,s^{-1}}$ spot reported by Walsh et al. (1998) was not redetected.

G23.657−00.127. The parallax of this source was measured by Bartkiewicz et al. (2008) and its value indicates that the circular distribution of masers has a linear radius of 405 AU, which differs significantly from the sizes inferred from the kinematic distances. The source was observed at three epochs (Tables 2, 4)
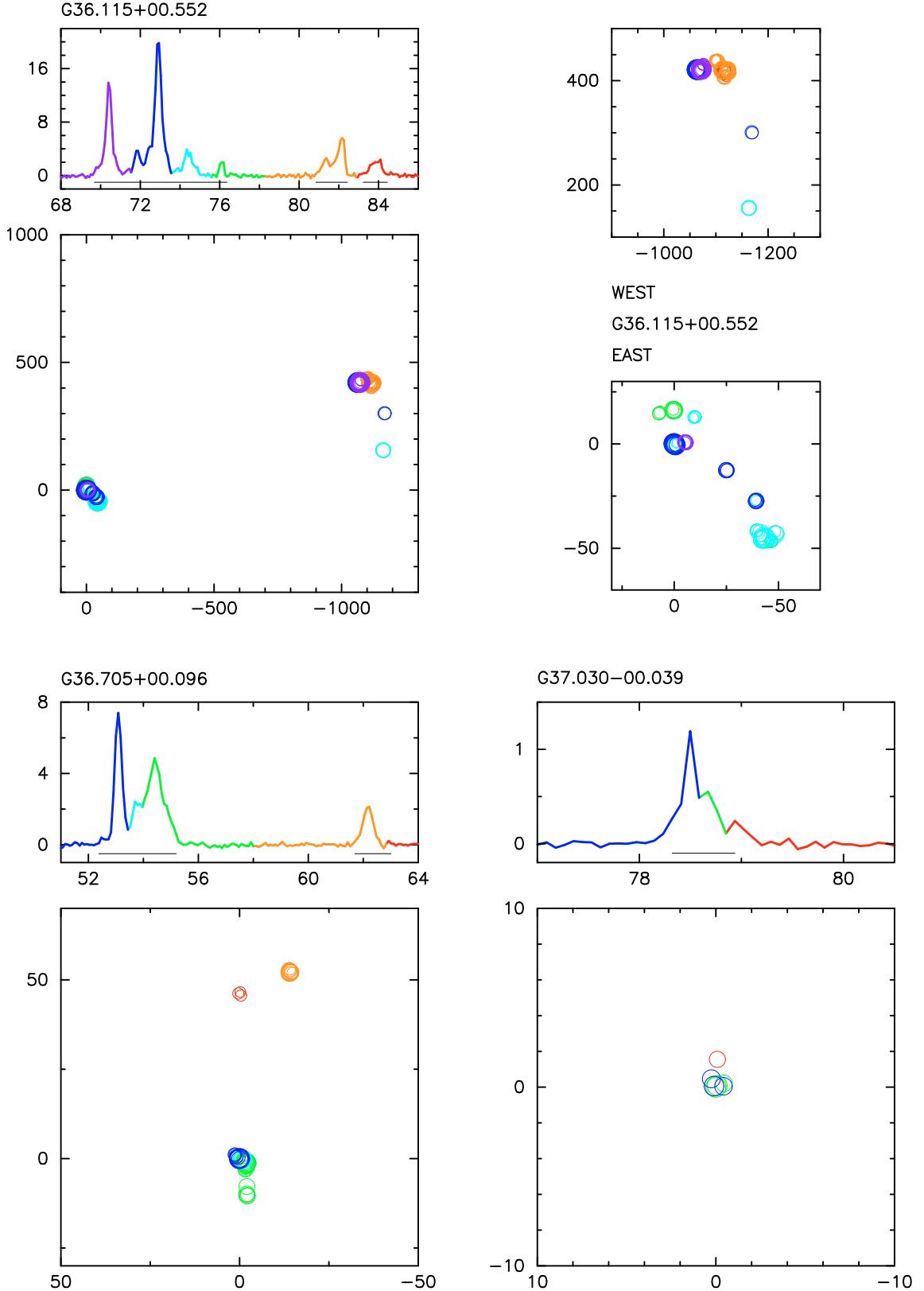
Fig. 1. continued.

and the ring-like morphology clearly persisted over time spans of 1.25 and 2.5 yr. A detailed description of the brightness variability in the source will be presented in a forthcoming paper.

G23.707−00.198. Walsh et al. (1998) detected 7 masers in a velocity range of 74.9−81.4 km s^{-1}, randomly scattered over

a 0.″15 area. The first epoch of EVN maps of this source (run 2) detected 23 clusters (140 spots) of which 19 form a 71 mas (corresponding to 360/750 AU for near/far kinematic distance, respectively) long arc in the NS direction, which has a velocity span of 8 km s^{-1}. A clear velocity gradient is seen in the overall
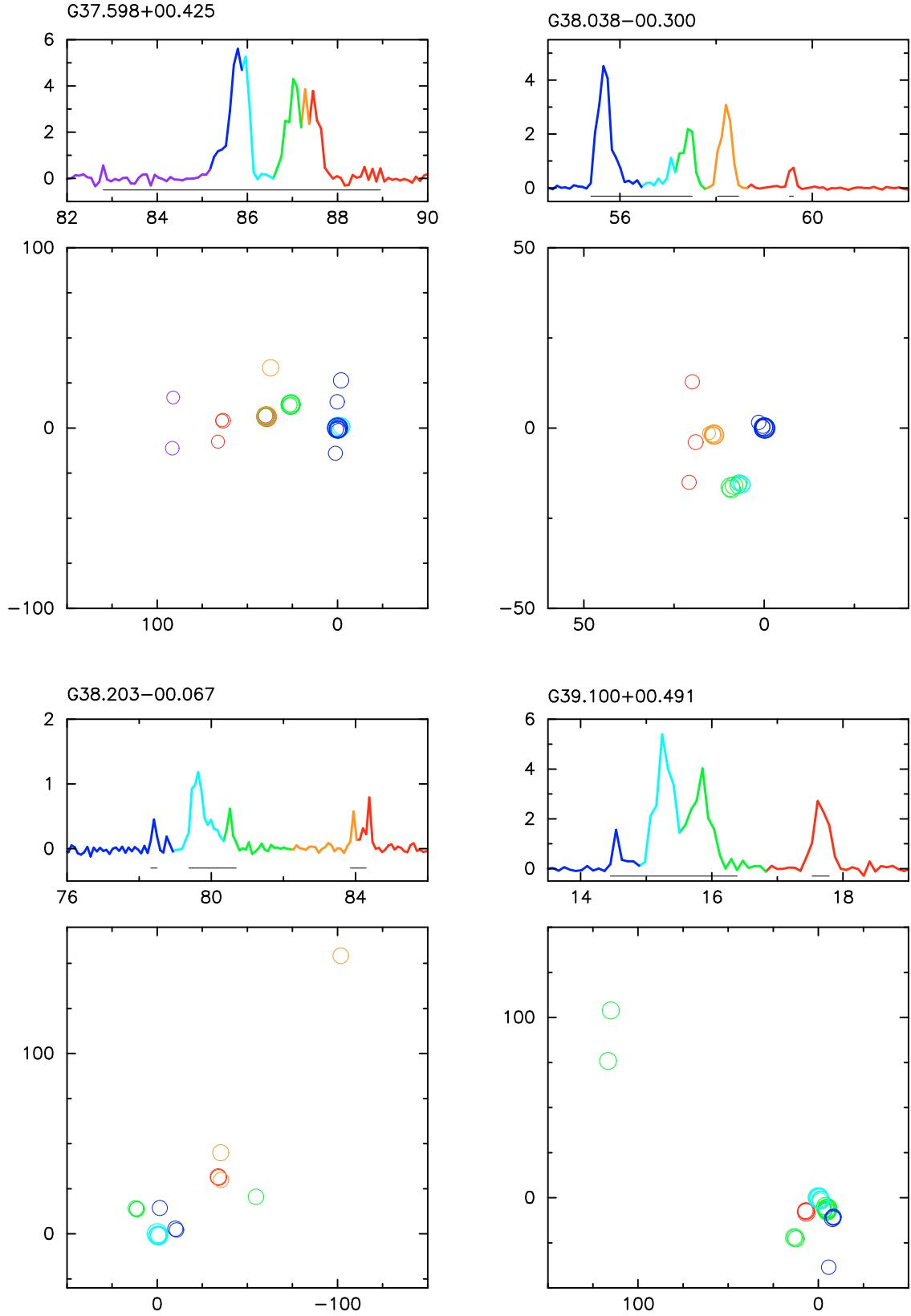
Fig. 1. continued.

arched distribution. The remaining clusters (all blue-shifted) are located ~100 mas to the west (two clusters) and ~20 mas to the east (two clusters), relative to the brightest spot. All four clusters are weak and were not detected at a later epoch (run 3a), but this data had poorer sensitivity. The brightest methanol maser

component (Table 5) coincides in position (within 82 mas) and velocity (within 0.1 km s^{-1}) with weak (60 mJy beam^{-1}) H$_2$CO maser emission at 4.8 GHz (Araya et al. 2006). We note that this is well within the absolute positional accuracy of the H$_2$CO maser. Both masers lie at the edges of two probable H II regions

Table 7. Results of VLA observations at 8.4 GHz.

| Radio continuum source | S_p | S_{int} | Size | | | Nearest maser | Separation |
| | | | Major axis | Minor axis | PA | | |
	(mJy beam^{-1})	(mJy)	($''$)	($''$)	($°$)		($''$)
G21.385−00.254	13.00	65	3.8	1.8	+50	G21.407−00.254	76.8
G24.148−00.009	1.05	1	0.6*	0.4*	+35	G24.148−00.009	0.11
G26.598−00.024	4.30	42	3.8	2.5	−35	G26.598−00.024	0.80
G28.817+00.365	0.81	0.8	0.6	0.5	−20	G28.817+00.365	0.08
G30.330+00.090	8.70	13	1.3	0.8	−25	G30.318+00.070	85.6
G31.160+00.045	2.40	22	2.0	1.5	+70	G31.156+00.045	11.9
G31.582+00.075	0.43	15	4.0	3.0	0	G31.581+00.077	9.00
G36.115+00.552	0.25	0.2	0.7*	0.3*	−45	G36.115+00.552	0.20

* Angular size upper limits (see Sect. 3.2).

Table 8. Parameters of ellipses fitted to the maser spot distributions.

| Source | Centre ΔRA, ΔDec.* | Semi-axes | | PA** | e |
	(mas, mas)	a (mas)	b (mas)	($°$)	
G23.207−00.377	−62, 71	126	45	−60	0.93
G23.389+00.185	−34, −75	95	56	+45	0.81
G23.657−00.127	−69, −93	133	128	−10	0.38
G24.634−00.324	−31, 17	45	15	−45	0.94
G25.411+00.105	61, 46	103	70	+90	0.73
G26.598−00.024	161, −73	192	111	−84	0.81
G31.047+00.356	−30, −15	37	18	+47	0.87
G33.980−00.019	−11, −18	42	20	+80	0.88
G34.751−00.093	9, −16	27	16	−83	0.80

* Coordinates relative to the brightest spots as listed in Table 5. ** The position angle of semi-major axis (north to east).

(Araya et al. 2006, their Fig. 2) with a peak intensity of 6.1 mJy beam^{-1} at 5 GHz (VLA C-configuration). Our VLA A-configuration data at 8.4 GHz do not show any emission above the 0.15 mJy beam^{-1} sensitivity limit, nor was this source detected at 8.6 GHz with a 2 mJy beam^{-1} limit (Walsh et al. (1998). Therefore, the H II regions are intrinsically weak at frequencies >5 GHz or they are possibly resolved at subarcsec angular resolution.

G25.411+00.105. Beuther et al. (2002) observed this source with the ATCA and found only two components at velocities of 94 and 97 km s^{-1} at positions that coincide to within $0\rlap{.}''2$ with the brightest spots in the EVN maps. We detected 30 spots, probably because of our ∼50 times higher sensitivity, although variability may also be involved. The distance of 9.5 kpc (Sridharan et al. 2002) implies that the linear radius of the ring distribution is 980 AU.

G26.598−00.024. The maser is located $0\rlap{.}''85$ from a cometary H II region (Fig. 2) with a spectral index of 0.23 between 1.4 and 5 GHz (Becker et al. 1994). This corresponds to linear distances of 1530(11 400) AU. The flux density of 4.4 mJy at 8.4 GHz, compared with 55 mJy at 5 GHz, implies that the turnover frequency is near 5 GHz. The methanol maser probably forms behind a shock front induced by the H II region. The strongest maser component, at 24.2 km s^{-1}, coincides in velocity with a 24.3 km s^{-1} absorption feature (−59.8 mJy) in the H$_2$CO line at 4.8 GHz (Sewilo et al. 2004).

G36.115+00.552. The brightest component of the NW maser structure is $0\rlap{.}''2$ away from the weak point continuum source at PA = 120° (Fig. 2). The shape of this complex suggests the existence of an outflow. However, the kinematics are not consistent with an outflow model (Sect. 4.2.3), nor do CO (2–1) line maps at 29$''$ resolution detect any molecular outflow (Zhang et al. 2005).

4. Discussion

4.1. Kinematic models of the origins of methanol masers

The diverse morphologies of methanol masers indicate that there is no straightforward explanation of the origin of this emission, as discussed previously (Norris et al. 1993; Phillips et al. 1998; Minier et al. 2000). The main hypotheses for the origin of methanol masers assume that they originate in a circumstellar disc or torus, in outflows or a shock colliding with a rotating molecular cloud. The results that we obtained by applying the existing models to our data are summarized below.

4.1.1. Rotating and expanding ring

Ring-like masers, which are prevalent in the present sample, may represent an inclined disc or torus around a massive protostar or young star. There is a tendency for flatter structures to have a larger velocity width, in all sources apart from G23.657−00.127, (see Table 5), which suggests that we observe the effects of inclination and all motion is intrinsic to the plane of the ring. To test this hypothesis, we applied the model of a rotating and expanding thin disc (Uscanga et al. 2008) to the nine ring-like masers. First, the coordinates of the spots (x_j, y_j) were transformed to a reference system (x'_j, y'_j) in which the origin was the center of the ellipse and the x'-axis was directed along the major axis of the projected ellipse (see Fig. 1 in Uscanga et al. 2008). We then attempted to reproduce the kinematics using the LSR velocities (V_{LSR}) of the maser spots to determine rotation (V_{rot}), expansion (V_{exp}), and systemic (V_{sys}) velocities of each source. The solutions were based on the minimisation of the χ^2_V function expressed in Eq. (8) by Uscanga et al. (2008)

$$\chi^2_V = \frac{1}{N-3} \sum_{j=1}^{N} \frac{1}{\sigma_V^2}\left(V_{\text{LSR},j} - V_{\text{sys}} - \frac{x'_j}{a}V_{\text{rot}}\sin i - \frac{y'_j}{a}V_{\text{exp}}\tan i\right)^2,$$

where σ_V was the spectral resolution of the observations corresponding to the uncertainty in the LSR velocity. The inclination angle is the angle between the line-of-sight and the normal to the ring plane, which is defined to be $i = \text{acos}(\frac{b}{a})$. The semi-major and semi-minor axes (a, b) were taken from Table 8. We note, that we cannot determine the sign of the inclination angle from the data available and the direction of the rotation is therefore ambiguous, nor distinguish between outflow and contraction. Additional information (e.g., spectroscopic and interferometric observations of molecular clouds at mas resolution) are necessary to solve these questions. For the purpose of the model, we assumed that the brightest and the most complex half of the ellipse is closer to the observer. The results of fitting are
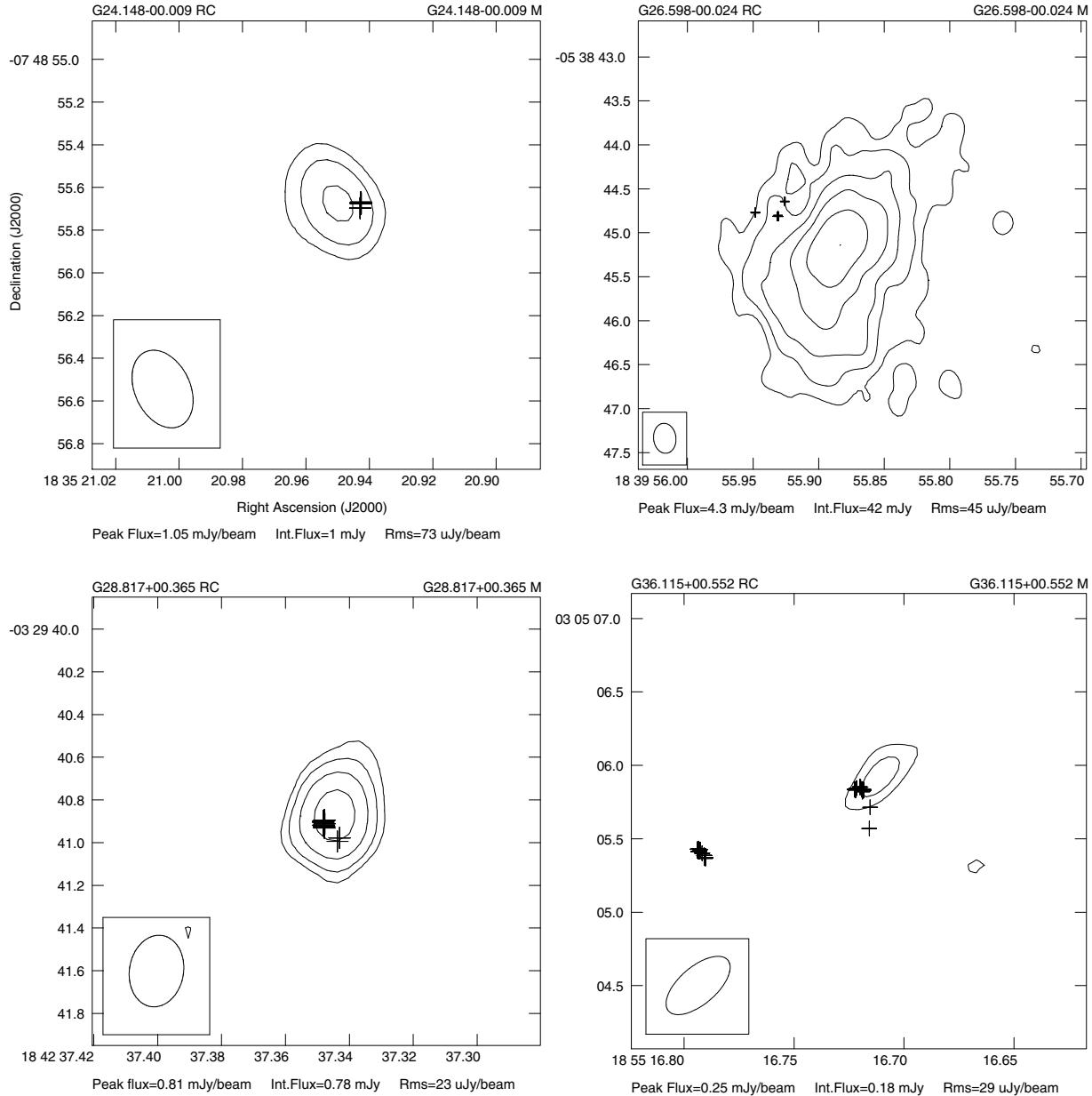
Fig. 2. The 8.4 GHz continuum emission towards four methanol maser sites taken using VLA on 2007 August 18. The names of radio continuum sources (RC) relate to the Galactic coordinates of their peak fluxes. The peak and integrated fluxes as well as the levels of rms ($1\sigma_{\rm rms}$) are given under each map and the beamsizes are presented at the left bottom corners. Contours trace the levels of $3\sigma_{\rm rms} \times (1, 2, 4, 8, 16, 32, 64, ...)$. Crosses represent the 6.7 GHz methanol maser spots registered using EVN.

summarized in Table 9 and an example of the fit of the model to the data, for G33.980−00.019, is presented in Fig. 4.

We note that in general the expansion/infall velocity is higher than the rotation component in the majority of sources, as can be clearly seen in the maser spot distributions (Fig. 1). If the rotation velocity was instead higher than that of expansion or infall, the extreme values of velocities could be produced where the major axis and ellipse intersect (at a position angle of 0° from the major axis). In four of nine sources, the opposite result is found that higher blue- or red-shifted velocities appear where the minor axes intersect the ellipses (see plots of G23.207−00.377, G23.389+00.185, G24.634−00.324, and G25.411+00.105). The average position angle of the most extreme velocity with respect to the major axis in all nine rings, and the standard dispersion in the mean, is $52° \pm 11°$. This suggests that the masers originate in the zone where the radial motions exist and

expansion/infall plays a role. This could occur at the interface between the disc/torus and outflow. A similar result was reported for the archetypical object Cep A (Torstensson et al. 2009), where the major axis of the elliptical distribution of 6.7 GHz methanol masers is perpendicular to the bipolar outflow. Their LSR velocity distributions show similar characteristics in that expansion or contraction dominates over the rotation.

4.1.2. Linear maser as edge-on disc?

A thin disc seen edge-on would appear to have a linear morphology. Norris et al. (1998) argued that maser radiation propagates most strongly in the plane of the disc due to the greater column depth, to explain why so many methanol masers with linear morphology appeared in the data then available.

Table 9. Parameters derived by fitting kinematics of the rotating and expanding disc model.

Source	V_{rot} (km s^{-1})	V_{exp} (km s^{-1})	V_{sys} (km s^{-1})	i ($°$)	χ_V^2
G23.207−00.377	−1.17	+3.96	79.46	−69	168
G23.389+00.185	−1.26	−1.71	74.91	+54	101
G23.657−00.127	+7.29	−2.61	81.90	+16	641
G24.634−00.324	+8.64	−2.25	38.96	+71	544
G25.411+00.105	+0.09	−1.17	95.84	+47	206
G26.598−00.024	+0.81	−0.81	24.58	−55	30
G31.047+00.356	+4 × 10^{-7}	−2.43	80.68	−61	211
G33.980−00.019	−0.45	+2.97	61.86	−62	123
G34.751−00.093	−1.17	−2.88	51.17	+53	22

The signs + and − of the rotation and expansion velocities refer to the clockwise or anti-clockwise rotation and outflow or inflow for positive i. Both rotation and flow are reversed in a case of negative i. For each source, both signs together with the sign of i could be reversed since our model does not give the directions unambiguously.
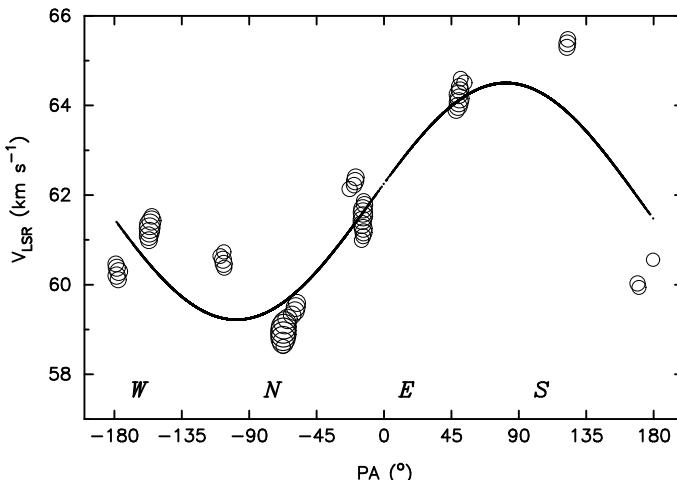
Fig. 4. Velocity of the maser spots in G33.980−00.019 versus azimuth angle measured from the major axis (north to east). The open circles represent the data and are proportional to the logarithm of the flux densities. The sinusoidal line represents the best-fit kinematical model of a rotating and expanding disc (with infintesimal thickness) using the parameters listed in Table 9.

We do not confirm this selection effect and note that the increased sensitivity detects more complex structures of masing regions. Only 16% of our sample are linear masers (compared to 29% ring-like masers) and they are also not the brightest, although it is possible that if there is strong expansion or infall, this would produce a steeper velocity gradient in edge-on discs and possibly make the masers fainter.

We calculated the mass that each linear maser structure would contain if it originated in a disc in Keplerian rotation, using a method similar to that of Minier et al. (2000). Assuming that the masing area corresponds to the diameter of the disc, the average central mass of these five linear structures is $0.12 M_\odot$ or $0.44 M_\odot$ for the near or far kinematic distances, respectively. These subsolar values are very unlikely for massive protostars. We agree with Minier et al. (2000) that the underlying assumption is wrong and we do not detect the full diameter of the disc. However, if we assume that the true extent of the linear masers is similar to the average size of the major axis of

the nine ellipses (188 mas), this implies a mean central mass of $76 M_\odot$ or $190 M_\odot$ for the near or far kinematic distance, respectively. These values seem unrealistically high. Another solution is that the masers are not bound by Keplerian rotation and we argue that the most likely explanation is that the linear morphology results from a different scenario. Linear structures with ordered velocity gradients may be produced readily by geometric effects in outflows. It seems significant that Szymczak et al. (2007) detected molecular line emission from HCO$^+$, CO, and CS towards these five sources using the IRAM 30 m telescope, supporting the outflow scenario. In addition, De Buizer et al. (2009) imaged SiO outflows towards five methanol masers with linear morphologies. They found that the spatial orientations of the outflows were inconsistent with the methanol masers tracing discs. Linear masers produced by outflows seemed to provide a much more plausible scenario. Finally, we also note that the linear masers have a smaller extent than most other maser structures (Table 5). In particular, the entire G35.793−00.175 structure is only 10 mas long corresponding to the typical size of an individual maser cluster in other sources. We conclude that most of the linear masers are more likely to be associated with outflows than with edge-on discs, although it is possible that more sensitive observations might indicate that some are part of ring-like or other structures. G25.411+00.105 (see Sect. 3.4) provides such an example, since Beuther et al. (2002) found only two maser spots, whilst in the present study we detected 30 spots, forming a ring-like morphology.

4.1.3. Propagating shock front

Dodson et al. (2004) proposed another model for linear methanol masers. A low speed planar shock propagating through the rotating molecular cloud would produce a linear spatial distribution of maser spots if the shock was propagating close to perpendicular to the line of sight. The linearity would be disrupted where the shock interacted with density perturbations in the star-forming regions. The main diagnostic for this scenario is the perpendicular orientation of velocity gradients within individual clusters with respect to the main large-scale velocity gradient. We analyzed the internal gradients of clusters and found this behaviour in three out of five masers with linear morphologies (G22.335−00.155, G23.966−00.109, and G30.318+00.070). In addition, the arched source, G33.641−00.228, shows similar characteristics in four (out of six) clusters, which have internal velocity gradients perpendicular to the longest axis of the overall structure. All these masers have young massive objects in close proximity less then 1″22 away (Sect. 4.2), which could be responsible for the external shocks. Proper motions studies are needed to verify this scenario.

4.1.4. Bipolar outflow

The bipolar outflow model for H$_2$O masers associated with a high-mass young stellar object was proposed by Moscadelli et al. (2000) and confirmed in IRAS20126+4104 by proper motion studies (Moscadelli et al. 2005). We also tested this model for all sources in this study. The assumptions of the model are as follows: masers originate in the surface of a conical bipolar jet due to the interaction between the ionised jet and the surrounding neutral medium, and the velocity of a maser spot, V_o, is directed radially outward from the central star at a constant value. The center of the coordinate system is at the vertex of the cone, the z-axis is along the line of sight, and the x-axis coincides with

Table 10. Parameters derived from fitting the biconical outflow model of Moscadelli et al. (2000).

Source	ΔRA, ΔDec.*	V_o	PA	Ψ	θ	χ^2
	(mas, mas)	(km s^{-1})	(^{o})	(^{o})	(^{o})	
G23.707−00.198	33, 45	−52.7	57	115	37	1.2
G24.541+00.312	−52, −15	−15.5	112	52	48	2.4

* Coordinates relative to the brightest spots as listed in Table 5.

the projection of the outflow on the plane of the sky (see Fig. 4 in Moscadelli et al. (2000)). Taking the central velocity of the maser emission (V_c) to be the systemic LSR velocity, we minimized the χ^2 function as expressed in Eq. (3) of Moscadelli et al. (2000)

$$\chi^2 = \sum_{j=2}^{n} \left(\frac{V_z^j}{V_z^1} - \frac{V_{LSR}^j - V_c}{V_{LSR}^1 - V_c} \right)^2,$$

where n is the number of spots, V_z^j is the velocity of the spot #j calculated using Eqs. (1) and (2) from Moscadelli et al. (2000), and V_{LSR}^j is the observed LSR velocity of the spot.

We obtained reasonable fits for only two of the arched sources, G23.707−00.198 and G24.541+00.312. The following best-fit model parameters are listed in Table 10: the position of the vertex, the opening angle of the cone (2θ), the inclination angle between the outflow axis and the z-axis (ψ), and the direction of the x-axis, PA, which is the position angle of the outflow on the plane of the sky. A comparison between the modelled and observed data and a sketch of the orientation of the outflow was presented previously in Fig. 1 in Bartkiewicz et al. (2006). It is significant that the vertices of the cones calculated for both sources coincide with infrared sources within the position uncertainties (Sect. 4.2). In addition, molecular line emission at similar LSR velocities was reported towards both sources (Szymczak et al. 2007). As we mentioned previously, Araya et al. (2006) imaged H$_2$CO maser emission at 4.8 GHz towards G24.541+00.312. All of these findings ensure that the outflow scenario is plausible for these two objects.

We tested the outflow model intensively on the four maser sources associated with HII regions. However, we did not achieve a reasonable fit that would place the vertex of the cone at the center of the radio continuum object, whilst reproducing the maser spot kinematics, for any of these sources.

4.2. Association with MIR emission

Early work by Szymczak et al. (2002) showed that ∼80% of methanol masers have infrared counterparts in IRAS and/or MSX catalogues. Since maser data with position accuracy as good or better than these IR catalogues (30″−5″) have become available, the fraction of secure identifications has diminished (Pandian et al. 2007). We can now attempt identifications with sub-arcsec resolution data.

We used *Spitzer* IRAC data to test the association between methanol masers and MIR emission. Images at 3.6, 4.5, 5.8, and 8.0 µm from the GLIMPSE survey, all at 0″6 resolution (Fazio et al. 2004), were retrieved from the *Spitzer* archive[3] and compared with the radio data using AIPS.


[3] http://irsa.ipac.caltech.edu/applications/Cutouts/
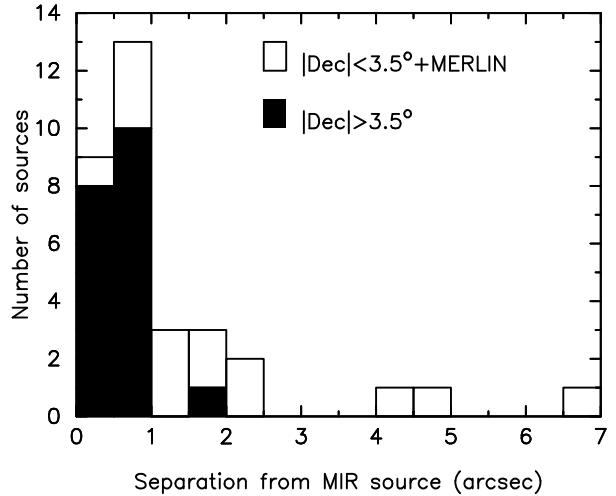
Fig. 5. Histogram of number of the methanol masers as a function of angular separation from associated MIR sources at 4.5 µm. Bin size is 0″5. The sources are divided into two groups with position measurements of high accuracy (|Dec.| > 3°5) and lower accuracy (|Dec.| <3°5 plus those measured with MERLIN alone).

The angular separation between the brightest maser spot of each source in our sample and the nearest MIR source at 4.5 µm (Δ_{MIR}) is given in Table 5 and a histogram of the results is shown in Fig. 5. The average separation for the entire sample is 1″18 ± 0″19 and the median value is 0″89, whereas, for the subsample of 19 objects at |Dec.| > 3°5 with coordinates measured using the EVN, the corresponding values are 0″61 ± 0″09 and 0″51, respectively. The remaining 14 targets with |Dec.| < 3°5, or with positions derived from the MERLIN data alone, show a larger Δ_{MIR} with the mean and median values of 1″96 ± 0″35 and 1″61, respectively. Since the images of these sources had poor *uv*-plane coverage and hence less accurate astrometry, we suggest that their higher estimates of Δ_{MIR} have a higher uncertainty and that most associations are also likely to be genuine.

We conclude that the majority of maser sources coincide, within ≲1″ with MIR emission, i.e., the maser emission from each source falls within one *Spitzer* pixel (nominal size ∼1″2, see Fazio et al. 2004) in the IRAC 4.5 µm image. This strongly reinforces the finding by Cyganowski et al. (2008), who reported coincidences to within ≲5″ for 46 out of 64 methanol sources with positions measured using the ATCA. Extended emission in the IRAC 4.5 µm band has been postulated to be a tracer of shocked molecular gas in protostellar outflows (e.g., Davies et al. 2007; Cyganowski et al. 2008 and references therein). This IRAC band contains H$_2$ and CO lines that may be excited by shocks. Using shock models, Smith & Rosen (2005) predicted that H$_2$ emission in outflows is 5–14 times stronger in the 4.5 µm band than in the 3.6 µm band. Cyganowski et al. (2008) identified more than 300 objects with extended 4.5 µm emission, which may relate to outflows in massive stars. Four maser sources from our sample, G23.966−00.109, G35.793−00.175, G37.479−00.105, and G39.100+00.491, were included in their catalogue.

In order to search for extended emission, we created images of the 4.5 µm−3.6 µm excess by subtracting the 3.6 µm image of each of our sources from its 4.5 µm counterpart, and compared these with the 4.5 µm image. All the sources have extended 4.5 µm emission. Figure 6 shows the 4.5 µm−3.6 µm excess superimposed on the 4.5 µm image for selected sources. Source G21.407−00.254 illustrates how the maser emission

located precisely inside the brightest pixel of the $4.5\,\mu m - 3.6\,\mu m$ image outside the $4.5\,\mu m$ peak. There is also evidence that maser clusters in at least three sources are associated with $4.5\,\mu m$ emission excess. The image at the position of G24.148−00.009 shows that the maser coincides exactly with maxima of both the $4.5\,\mu m - 3.6\,\mu m$ excess and of the $4.5\,\mu m$ emission. Weak, extended $4.5\,\mu m$ emission is also seen at the edges of two neighbouring sources and in diffuse lanes. The maser G37.598+00.425 coincides with a maximum in a very asymmetric distribution of $4.5\,\mu m - 3.6\,\mu m$ emission excess that is displaced by $\sim 1\rlap{.}''5$ from a peak of $4.5\,\mu m$ emission, implying that the methanol maser and the excess in the $4.5\,\mu m$ IRAC band are very strongly related. Similar evidence is provided by G38.203−00.067, where the maser is offset by more than $8''$ from a bright MIR object. The maser is $\sim 1\rlap{.}''7$ away from a weak bump in a large lane of diffuse $4.5\,\mu m - 3.6\,\mu m$ emission excess. Inspection of IRAC images for other bands suggests that the maser is probably associated with a faint MIR object.

All the counterparts in the sample have MIR properties typical of embedded young massive objects (e.g., Kumar et al. 2007) associated with the methanol masers (Ellingsen 2006). We defer a detailed discussion of the MIR spectral indices of individual objects, because several bright sources (e.g., G23.389+00.185, G23.657−00.127, and G24.634−00.324) are saturated in the IRAC images, while for others only upper limits to the $3.6\,\mu m$ flux can be derived (e.g., G23.966−00.109, G37.030−00.039, and G38.203−00.067). We note only, that the MIR objects associated with methanol masers that have a ring-like morphology have much stronger emission at $8\,\mu m$, and all the objects that are saturated in the IRAC images have regular maser structures. In contrast, no object saturated in the IRAC images has a complex maser morphology. This suggests that the MIR counterparts of masers with less regular structures are deeply embedded massive stars that are younger than the counterparts of those with more regular, ring-like maser structures. One can speculate that in those younger objects the methanol maser originates in a limited number of confined regions, whilst more regular structures emerge during later evolutionary stages.

In summary, we have found strong evidence of a close coincidence of 6.7 GHz methanol masers with $4.5\,\mu m$ emission excess. This provides a firm argument that methanol emission originates in those inner parts of an outflow or disc/torus where the molecular gas is shocked.

This hypothesis is strongly supported by the kinematic model that can be successfully applied to the ring masers in our sample, which involved a rotating and expanding disc wherein expansion dominates the velocity field. Moreover, a fraction of masers seem to fit the model of a bipolar jet or that of a shock front colliding with the surrounding molecular material.

5. Conclusions

We have completed a 6.7 GHz methanol line imaging survey of 33 maser sources in the Galactic plane. High quality EVN images were obtained for 31 targets showing their mas-scale structures, from which we derived the absolute positions of 29 sources with a few mas accuracy. In most cases, the masers exhibit complex structures. The observed morphologies can be divided into five groups: simple, linear, ring-like, complex, arched, and pair. It is surprising that about 29% of the sources exhibit ring-like distributions of maser spots that were not apparent in previous VLBI surveys, which were less sensitive and concentrated on brighter masers. We find that many of the other ordered structures, notably linear and arched, can be interpreted

as originating from the interaction between collimated or biconical outflows and the surrounding medium.

A simultaneous survey at high angular resolution of continuum emission at 8.4 GHz towards the maser targets revealed that only 16% of the methanol masers appear to be physically related to H II regions. In three cases, the maser coincides with a peak in a compact and relatively weak continuum object. These are believed to be young UC H II regions. In general, these results seem to imply that 6.7 GHz methanol masers appear before the ionised region is detectable at cm wavelengths. The hypothesis that these masers are possible associated with HC H II regions needs to be verified.

We used the *Spitzer* GLIMPSE survey to demonstrate that the majority of methanol masers are closely associated with MIR emission. Analyzis of the MIR counterparts suggests that masers with a regular, ring-like morphology are associated with more evolved proto- or young stars, relative to the counterparts of masers with more complex, irregular structures. Moreover, both the kinematics of the masers with a ring-like distribution and the characteristics of associated MIR emission are consistent with a scenario in which the methanol emission is produced by shocked material associated with a disk or torus, possibly from an interaction with the outflow.

References

Araya, E., Hofner, P., Goss, W. M., et al. 2006, ApJ, 643, L33
Bartkiewicz, A., Szymczak, M., & van Langevelde, H. J. 2004, PoS, Proceeding of the 7th European VLBI Network Symposium, ed. R. Bachiller, F. Colomer, J. F. Desmurs, & P. de Vincente, Toledo, Spain, 187
Bartkiewicz, A., Szymczak, M., & van Langevelde, H. J. 2005, A&A, 442, L61
Bartkiewicz, A., Szymczak, M., & van Langevelde, H. J. 2006, PoS, Proceedings of the 8th European VLBI Network Symposium, ed. A. Marecki, 039
Bartkiewicz, A., Brunthaler, A., Szymczak, M., van Langevelde, H. J., & Reid, M. J. 2008, A&A, 490, 787
Bartkiewicz, A., Szymczak, M., & van Langevelde, H. J. 2009, PoS, Proceedings of the 9th European VLBI Network Symposium, ed. F. Montovani, 037
Becker, R. H., White, R. L., Helfand, D. J., & Zoonematkermani, S. 1994, ApJS, 91, 347
Beuther, H., Walsh, A., Schilke, P., et al. 2002, A&A, 390, 289
Caswell, J. L., Vaile, R. A., Ellingsen, S. P., Whiteoak, J. B., & Norris, R. P. 1995, MNRAS, 272, 96
Cragg, D. M., Sobolev, A. M., & Godfrey, P. D. 2002, MNRAS, 331, 521
Cyganowski, C. J., Whitney, B. A., Holden, E., et al. 2008, AJ, 136, 2391
Dartois, E., Schutte, W., Geballe, T. R., et al. 1999, A&A, 342, L32
De Buizer, J. M., & Minier, V. 2005, ApJ, 628, L151
De Buizer, J. M., Redman, R. O., Longmore, S. N., Caswell, J., & Feldman, P. A. 2009, A&A, 493, 127
Davis, C. J., Kumar, M. S. N., Sandell, G., et al. 2007, MNRAS, 374, 29
Diamond, P. J., Garrington, S. T., Gunn, A. G., et al. 2003, MERLIN USer Guide, Ver. 3
Dodson, R., Ojha, R., & Ellingsen, S. P. 2004, MNRAS, 351, 779
Ellingsen, S. P. 2006, ApJ, 638, 241

Fazio, G. G., Hora, J. L., Allen, L. E., et al. 2004, ApJS, 154, 10
Fitzgibbon, A., Pilu, M., & Fisher, R. B. 1999, IEEE Transactions on Pattern Analysis and Machine Intelligence, 21, 476
Kumar, M. S. N., & Grave, J. M. C. 2007, A&A, 472, 155
Longmore, S. N., Burton, M. G., Barnes, P. J., et al. 2007, MNRAS, 379, 535
Menten, K. M. 1991, ApJ, 380, L75
Menten, K. M., Reid, M. J., Pratap, P., Moran, J. M., & Wilson, T. L. 1992, ApJ, 401, L39
Minier, V., Booth, R. S., & Conway, J. E. 2000, A&A, 362, 1093
Moscadelli, L., Cesaroni, R., & Rioja, M. J. 2000, A&A, 360, 663
Moscadelli, L., Menten, K. M., Walmsley, C. M., & Reid, M. J. 2002, ApJ, 564, 813
Moscadelli, L., Cesaroni, R., & Rioja, M. J. 2005, A&A, 438, 889
Norris, R. P., Whiteoak, J. B., Caswell, J. L., Wieringa, M. H., & Goigh, R. G. 1993, ApJ, 412, 222
Norris, R. P., Byleveld, S. E., Diamond, P. J., et al. 1998, ApJ, 508, 275
Pandian, J. D., & Goldsmith, P. F. 2007, ApJ, 669, 435
Pestalozzi, M. R., Elitzur, M., Conway, J. E., & Booth, R. S. 2004, ApJ, 603, L113

Philips, C. J., Norris, R. P., Ellingsen, S. P., & McCulloch, P. M. 1998, MNRAS, 300, 1131
Sewilo, M., Watson, C., Araya, E., et al. 2004, ApJS, 154, 553
Smith, M. D., & Rosen, A. 2005, MNRAS, 357, 1370
Sridharan, T. K., Beuther, H., Schilke, P., Menten, K. M., & Wyrowski, F. 2002, ApJ, 566, 931
Szymczak, M., Hrynek, G., & Kus, A. J. 2000, A&ASS, 143, 269
Szymczak, M., Kus, A. J., Hrynek, G., Kepa, A., & Pazderski, E. 2002, A&A, 392, 277
Szymczak, M., Pillai, T., & Menten, K. M. 2005, A&A, 434, 613
Szymczak, M., Bartkiewicz, A., & Richards, A. M. S. 2007, A&A, 468, 617
Uscanga, L., Gomez, Y., Raga, A. C., et al. 2008, MNRAS, 390, 1127
Torstensson, K., van Langevelde, H. J., Vlemmings, W., & van der Tak, F. 2009, PoS, Proceedings of the 9th European VLBI Network Symposium, ed. F. Montovani, 39
Walsh, A. J., Burton, M. G., Hyland, A. R., & Robinson, G. 1998, MNRAS, 301, 640
van der Walt, D. J., Sobolev, A. M., & Butner, H. 2007, A&A, 464, 1015
Zhang, Q., Hunter, T. R., Brand, J., et al. 2005, ApJ, 625, 864

Table 1. Summary of previous high angular resolution studies of 6.7 GHz methanol masers.

Survey	Telescope	Spectral resolution (km s^{-1})	Angular resolution (mas)	$1\sigma_{rms}$ (mJy beam^{-1})	Number of targets	Median peak flux density (Jy)
Norris et al. (1993)	ATCA	0.3	1500	~500	15	475
Phillips et al. (1998)	ATCA	0.35	1500	~50	33	41
Walsh et al. (1998)	ATCA	0.18	1500	300	97	23
Minier et al. (2000)	EVN	0.04	few	$-^*$	14	272
Dodson et al. (2004)	LBA	0.2	5.3	2	5	148
This paper	EVN	0.09; 0.18	~6 × 14	3−12	31	3.6

* The value not given.

Table 2. Sample of methanol masers observed with the EVN. The names are the Galactic coordinates of the brightest spot of each target obtained in post-processing EVN data. The dates of each observing run are listed in Table 4. The phase-calibrator names and angular separations from the targets are given.

Source Gll.lll ± bb.bbb	Observing run	Phase-calibrator	Separation (°)
G21.407−00.254	3a	J1825−0737	3.1
G22.335−00.155	3a	J1825−0737	2.5
G22.357+00.066[1]	4a	J1825−0737	2.3
G23.207−00.377	2	J1825−0737	2.6
G23.389+00.185	2	J1825−0737	2.1
G23.657−00.127	2	J1825−0737	2.4
	3a	J1825−0737	2.4
	4a	J1825−0737	2.4
G23.707−00.198	2	J1825−0737	2.5
	3a	J1825−0737	2.5
G23.966−00.109	3a	J1825−0737	2.5
G24.148−00.009	3a	J1825−0737	2.4
G24.541+00.312	2	J1825−0737	2.4
G24.634−00.324	4a	J1825−0737	2.9
G25.411+00.105[2]	4a	J1825−0737	3.1
G26.598−00.024	4a	J1825−0737	4.1
G27.221+00.136	2	J1825−0737	4.5
G28.817+00.365	4b	J1834−0301	2.2
G30.318+00.070	4b	J1834−0301	3.2
G30.400−00.296	4b	J1834−0301	3.5
G31.047+00.356	4b	J1834−0301	3.5
G31.156+00.045	4b	J1834−0301	3.8
G31.581+00.077	4b	J1834−0301	4.1
G32.992+00.034[2]	4c	J1907+0127	4.2
G33.641−00.228	1	J1907+0127	3.5
G33.980−00.019	4c	J1907+0127	3.5
G34.751−00.093	4c	J1907+0127	3.0
G35.793−00.175	1	J1907+0127	2.7
G36.115+00.552	1	J1907+0127	3.4
	4c	J1907+0127	3.0
G36.705+00.096	4c	J1907+0127	3.1
G37.030−00.039	3b	J1856+0610	2.6
G37.479−00.105	3b	J1856+0610	2.4
G37.598+00.425	3b	J1856+0610	1.9
G38.038−00.300	3b	J1856+0610	2.2
G38.203−00.067	3b	J1856+0610	2.0
G39.100+00.491	3b	J1856+0610	1.2

[1] Source from Walsh et al. (1998).
[2] Sources from Beuther et al. (2002).

Table 3. Targets not detected with the MERLIN single baseline. The source names, coordinates, and peak flux velocities are taken from Szymczak et al. (2002).

Source Gll.ll ± bb.bb	RA, Dec. (J2000)	$V_{\rm p}$ (km s^{-1})
G21.57−00.03	18 30 36.5, −10 06 43	+117
G22.05+00.22	18 30 35.7, −09 34 26	+54
G24.93+00.08	18 36 29.2, −07 05 05	+53
G26.65+00.02	18 39 51.8, −05 34 52	+107
G27.21+00.26	18 40 03.8, −04 58 09	+9
G27.78+00.07	18 41 47.5, −04 33 11	+112
G28.02−00.44	18 44 02.1, −04 34 14	+17
G28.40+00.07	18 42 54.5, −04 00 04	+69
G28.53+00.12	18 42 57.7, −03 51 59	+25
G28.69+00.41	18 42 13.6, −03 35 07	+94
G28.85+00.50	18 42 12.8, −03 24 26	+83
G29.31−00.15	18 45 23.1, −03 17 23	+48
G33.74−00.15	18 53 26.9, +00 39 01	+54
G33.86+00.01	18 53 05.2, +00 49 36	+67
G34.10+00.01	18 53 31.9, +01 02 26	+56
G37.53−00.11	19 00 14.4, +04 02 35	+50
G38.12−00.24	19 01 47.6, +04 30 32	+70
G38.26−00.08	19 01 28.7, +04 42 02	+16

Table 6. Maser clusters towards 31 sources. If a spectrum of a maser cluster does not show a Gaussian profile we enter the sign − in the Cols. of *FWHM* and S_{amp}.

V_{LSR} (km s^{-1})	ΔRA (mas)	ΔDec. (mas)	S_p (mJy beam^{-1})	*FWHM* (km s^{-1})	S_{amp} (mJy beam^{-1})
G21.407−00.254					
89.040	0.0000	0.0000	2762	0.32	2672
89.303	−0.0192	9.7250	1426	0.35	1513
90.094	−8.9947	−26.3260	307	0.18	308
91.148	−136.3023	5.0420	891	0.26	888
91.412	−13.1560	−23.6830	117	−	−
91.587	−27.3535	1.5320	422	0.26	420
G22.335−00.155					
35.626	0.0000	0.0000	1714	0.32	1642
38.174	−10.9782	−47.4060	125	0.53	125
G22.357+00.066					
79.708	0.0000	0.0000	10 544	0.37	11 350
80.235	1.0074	−6.0100	10 067	0.47	10 190
81.114	2.8964	−18.3490	1422	0.48	1497
81.465	155.0868	−46.3230	492	−	−
83.574	139.2789	−18.6790	309	−	−
84.101	141.5278	66.5690	156	0.58	158
84.804	132.0327	75.7690	176	−	−
88.143	55.7575	208.5390	602	0.27	636
88.494	68.1772	277.2010	250	−	−
88.670	56.6464	207.5440	476	−	−
G23.207−00.377					
72.553	−101.3966	−64.2970	141	0.31	140
73.959	−32.5775	−17.5310	194	0.28	190
75.190	0.5751	9.9430	226	0.23	223
75.014	−25.7012	−1.9800	421	0.83	374
75.453	−269.6437	26.1920	893	0.34	946
75.629	57.3581	41.8210	647	0.34	683
76.069	−30.8269	−11.6140	229	0.42	228
76.596	−11.6581	3.1990	4748	0.43	4761
77.123	0.0000	0.0000	9292	0.34	9468
77.475	29.4751	−4.2880	3387	0.46	3463
77.739	11.0845	4.9910	3096	0.47	2852
78.793	53.0729	−33.4270	541	0.44	563
78.881	−217.1237	30.9130	286	0.28	293
78.969	47.4388	−30.9230	577	−	−
79.233	50.4581	−32.3460	1319	0.38	1412
79.496	−135.9039	−191.481	0 277	0.21	294
79.672	−113.8403	−117.084	0 213	0.41	221
79.936	−57.8547	−71.4830	315	0.29	303
80.727	−163.9145	−147.143	0 7092	0.36	6989
81.869	−136.2582	−139.260	0 8967	0.37	8838
81.869	−141.0800	−140.772	0 5874	0.60	5918
82.045	−157.2072	−145.562	0 1104	0.25	1119
82.836	−151.9599	−147.620	0 1190	0.43	1012
84.858	−47.3987	−112.077	0 791	0.56	679
G23.389+00.185					
72.641	−78.2268	32.6440	6398	0.46	6279
73.784	52.4158	32.4260	9326	0.47	8831
74.399	46.8761	38.8880	2978	0.41	2715
74.575	−43.2789	31.9400	4700	0.28	4730
74.750	43.4540	63.9750	311	−	−
74.750	41.0708	14.0150	267	−	−
74.838	31.5347	70.8960	19723	0.71	21320
74.926	41.8691	49.9560	1272	0.17	1232
75.453	0.0000	0.0000	21554	0.26	21587
75.541	−57.2121	153.9020	397	−	−

Table 6. continued.

V_{LSR}	ΔRA	ΔDec.	S_{p}	*FWHM*	S_{amp}
(km s^{-1})	(mas)	(mas)	(mJy beam^{-1})	(km s^{-1})	(mJy beam^{-1})
75.805	−64.5014	143.6490	3708	0.32	3768
76.069	78.5948	144.9390	6571	0.37	6686
76.332	−93.2091	154.8360	4516	0.62	4683
76.596	−70.0292	145.2360	1072	0.55	1086
76.948	20.9791	75.4450	721	0.31	727
77.035	−69.1893	147.1100	4860	0.28	4795
77.475	−73.8030	150.8570	234	0.19	234
77.563	−31.8834	157.9720	485	0.24	470
G23.657−00.127					
77.563	−5.0421	229.8720	816	0.42	754
77.563	−22.2581	232.7000	333	0.25	355
78.266	−71.1275	228.1640	1059	0.52	932
78.881	54.5928	171.6190	336	0.50	305
79.584	105.3428	117.0720	162	0.75	170
80.024	−124.7437	212.4980	1595	0.23	1607
80.112	−39.3568	213.5540	977	0.32	938
80.639	21.7712	−13.2960	850	0.49	691
80.727	14.3113	−66.4860	375	0.20	391
80.990	−156.9775	−5.2880	124	0.25	135
81.166	2.9967	−47.4670	362	0.30	370
81.166	26.3472	−70.2780	68	0.55	77
81.518	7.2432	−3.7020	588	0.42	564
81.781	46.3136	156.5250	126	0.39	117
81.869	10.2711	10.8770	806	0.30	820
81.869	13.2471	−13.0970	90	0.19	92
82.133	−1.5481	−43.7250	132	0.31	124
82.309	44.5072	156.8130	393	0.28	391
82.573	0.0000	0.0000	3623	0.48	3401
82.836	41.5298	162.2880	168	0.29	174
83.100	−210.9484	11.3450	182	0.24	196
83.276	−47.8646	−35.5030	1018	0.33	1036
83.539	69.2069	83.7510	80	0.27	81
83.979	0.7674	18.7780	143	0.62	125
83.979	−52.8072	−32.5950	557	0.58	531
84.243	−133.7606	−4.1400	358	0.27	373
84.858	45.6887	140.0160	548	0.44	552
86.264	−17.8008	−15.6640	797	0.37	766
86.791	−19.7200	−18.7010	746	0.37	702
87.231	−16.7410	−26.9680	96	0.24	96
87.670	−20.3523	−29.5260	280	0.26	272
G23.707−00.198					
58.578	20.4283	18.1540	377	−	
71.410	−101.2879	0.5490	200	0.19	207
71.762	−105.4053	−5.6330	128	0.19	141
72.993	−10.2000	57.1700	667	0.23	707
73.344	−1.6921	33.7300	92	0.40	95
73.608	0.3488	27.4820	100	0.22	102
74.223	−3.2461	38.1980	672	0.38	683
74.575	0.3933	23.6850	1845	0.26	1756
75.102	−0.0089	29.0830	404	0.47	416
75.190	16.6285	−9.9600	306	0.52	340
75.629	0.3577	26.8210	249	0.50	260
76.157	0.9722	19.8400	3319	0.46	3297
76.596	0.9589	17.6580	2054	0.83	2033
77.299	0.8772	16.2390	3473	0.29	3625
78.266	−14.6856	−14.3980	219	0.31	219
78.530	−13.7935	−14.4180	358	0.32	366

Table 6. continued.

V_{LSR} (km s^{-1})	ΔRA (mas)	ΔDec. (mas)	S_p (mJy beam^{-1})	*FWHM* (km s^{-1})	S_{amp} (mJy beam^{-1})
77.651	−0.4334	3.7530	2234	0.70	2239
78.090	−0.5982	1.0340	2144	0.95	2099
79.145	0.0000	0.0000	6059	0.79	5368
79.496	−17.3246	−13.9080	117	0.61	109
80.112	−14.3234	−14.3790	202	0.36	200
80.903	−4.2421	−8.0300	142	0.48	129
81.078	−3.9200	−8.6280	159	0.56	153
G23.966−00.109					
67.428	21.9498	−23.0050	387	0.30	369
68.219	23.3000	−22.9600	431	0.41	404
70.942	0.0000	0.0000	5487	0.41	5390
G24.148−00.009					
17.441	4.3548	−21.7190	1048	0.20	1048
17.529	0.1980	−0.0970	2459	0.51	2493
17.792	0.0000	0.0000	3648	0.40	3702
18.407	0.6149	5.9860	240	0.33	235
G24.541+00.312					
103.754	−35.7935	59.5820	233	0.23	233
105.688	0.0000	0.0000	7753	0.34	7453
106.215	−38.6463	37.3600	316	0.29	278
107.973	−10.8681	7.8090	238	0.33	239
106.479	−5.5553	2.9680	2788	0.49	2554
107.270	0.0253	1.0010	2700	0.47	2677
107.533	−1.8840	2.4950	2005	0.38	2052
108.324	94.8606	14.3270	106	0.32	108
108.588	−26.0490	13.4890	638	0.37	534
109.467	−39.7491	16.3690	339	0.57	339
109.643	−39.9396	16.9440	407	0.38	413
110.082	−41.4218	18.0810	728	0.39	742
G24.634−00.324					
34.725	−18.6698	25.4370	457	−	−
35.428	0.0000	0.0000	3027	0.29	3544
43.862	−62.2684	36.4860	2370	0.56	2322
45.795	−41.9147	45.7150	257	0.41	257
46.322	−43.8591	45.1230	312	0.38	313
47.904	−42.4775	45.4230	136	0.54	136
G25.411+00.105					
93.765	34.1096	111.2790	142	−	−
94.117	109.0956	−19.4400	82	−	−
94.820	115.8608	101.1940	847	−	−
94.644	−16.7363	86.3980	2374	0.51	2345
94.820	−3.5683	−20.6650	1025	0.50	1037
96.928	−3.5146	123.8050	323	−	−
96.928	3.2029	−5.4840	2251	0.42	2241
97.104	−46.6480	16.7050	2468	0.28	2504
97.280	0.0000	0.0000	3433	0.56	3690
98.861	176.2362	50.0100	139	−	−
G26.598−00.024					
22.952	2.1488	−0.1130	182	0.45	183
24.182	0.0000	0.0000	3043	0.34	3239
24.709	84.5157	−169.5700	1368	0.44	1276
25.061	335.4955	−131.1280	714	0.51	671
25.588	78.8583	−159.7380	76	−	−
25.939	338.8875	−124.8040	97	0.94	99

Table 6. continued.

V_{LSR} (km s^{-1})	ΔRA (mas)	ΔDec. (mas)	S_p (mJy beam^{-1})	*FWHM* (km s^{-1})	S_{amp} (mJy beam^{-1})
G27.221+00.136					
105.424	−11.6570	77.8590	253	0.42	237
106.391	−11.2849	77.8360	94	0.59	91
107.182	−33.2614	55.4880	245	0.42	232
109.731	−33.8577	32.9640	1239	0.26	1193
110.258	−34.2955	34.2190	1182	0.43	1179
111.225	−33.0149	35.1860	467	0.30	466
112.280	−19.4363	27.0680	563	0.35	538
112.719	−18.6697	27.1140	906	0.29	917
114.828	−20.1700	27.8700	166	0.25	169
115.268	−18.4171	23.1670	150	0.39	152
115.444	−19.0119	24.4340	158	−	−
115.707	−24.1941	47.1650	236	0.31	225
116.586	−24.7798	7.8580	437	0.23	457
117.114	−53.1908	8.6200	6519	0.33	6591
117.729	8.9344	−12.1430	448	0.23	469
117.817	−54.3145	7.6670	5642	0.55	5621
118.168	−9.3558	−11.4900	1991	0.33	1990
118.432	−55.3082	7.0300	4831	0.35	4755
118.783	0.0000	0.0000	12535	0.39	12021
118.959	−8.6878	13.1750	765	0.67	801
119.223	−70.7368	−6.8450	209	−	−
119.311	−9.2317	−5.7490	232	0.33	224
119.311	−34.3642	4.9240	135	0.51	111
119.750	−9.4066	11.3470	101	0.38	103
120.365	−15.4465	−18.4780	536	0.23	536
120.190	−20.1998	41.8670	1339	0.40	1367
121.069	−17.4294	44.0510	218	0.29	218
G28.817+00.365					
87.735	−73.2105	−56.0600	325	0.51	331
88.087	−63.9892	−72.9580	183	−	−
90.723	0.0000	0.0000	3137	0.36	3211
91.074	2.8641	17.4230	1440	0.62	1440
91.250	2.7787	3.5790	896	0.68	933
91.601	4.0115	20.0900	2511	0.31	2755
92.129	−3.1337	10.3800	743	0.47	761
92.656	−2.7143	26.7830	2116	0.38	2103
G30.318+00.070					
35.192	−23.8385	22.6390	300	0.53	303
36.070	0.0000	0.0000	514	0.68	528
36.949	5.6770	−5.0420	144	0.70	144
G30.400−00.296					
98.104	4.4898	−11.8250	2139	0.31	2151
98.455	0.0000	0.0000	2765	0.32	3129
100.388	−31.0281	−45.2180	1581	0.29	1603
101.618	−27.7091	85.7960	331	0.72	326
103.727	−19.1733	86.2030	1914	0.41	1923
103.727	67.4799	134.7790	497	0.28	503
104.430	66.4200	135.2860	260	0.43	267

Table 6. continued.

V_{LSR} (km s^{-1})	ΔRA (mas)	ΔDec. (mas)	S_p (mJy beam^{-1})	*FWHM* (km s^{-1})	S_{amp} (mJy beam^{-1})
G31.047+00.356					
81.058	−59.6159	−28.5990	277	−	−
78.070	−0.9674	7.7850	281	0.82	267
79.125	−1.2973	3.2920	1169	0.73	1180
80.179	0.4664	1.5320	544	0.55	555
80.882	0.0000	0.0000	1989	0.55	1960
81.058	−0.3989	−1.5250	1563	0.55	1568
82.991	−47.8577	−6.9740	617	0.28	651
84.045	−25.8591	9.6530	101	−	−
G31.581+00.077					
95.643	0.0000	0.0000	2722	0.35	2891
97.752	−60.9387	57.6080	349	−	−
98.104	37.3458	−7.0480	809	0.31	814
98.455	32.2616	−3.7570	376	0.39	386
98.631	149.7072	94.0260	493	−	−
98.806	−61.9691	79.9160	292	0.41	321
98.806	149.8767	93.2150	2045	0.68	2039
99.509	158.1329	69.4150	358	−	−
99.685	151.6794	56.5090	1099	0.39	1223
G32.992+00.034					
89.724	13.3545	−44.5810	321	−	−
90.339	−51.5775	49.8690	396	−	−
90.602	14.7555	−34.4810	1967	0.40	1953
90.954	26.7960	1.1600	4650	0.32	4838
91.393	−4.7370	−6.0210	493	0.50	505
91.481	28.3665	0.9760	1856	0.50	1867
91.656	−16.1355	37.9820	465	−	−
91.832	0.0000	0.0000	6212	0.35	6786
92.184	34.7340	−14.9630	394	0.28	394
92.447	35.5635	−14.7320	163	−	−
92.711	24.9990	−19.6750	199	−	−
94.204	51.0915	−1.6040	600	0.26	574
94.731	49.8900	−4.5590	445	0.22	446
G33.641−00.228					
58.840	0.0000	0.0000	28300	0.31	29569
59.540	−9.5996	−12.3000	4105	0.29	4259
59.800	−14.3994	−20.1000	12260	0.22	12665
60.330	69.5970	−15.9000	20402	0.30	21448
60.420	61.9473	−25.9000	2280	0.50	2688
60.510	60.8973	−27.0000	1621	−	−
60.860	13.3494	−28.6000	1672	0.30	1716
60.940	65.3971	−14.6000	10447	0.35	10558
61.120	76.3467	−2.3000	356	0.35	372
61.300	56.2475	−17.0000	207	0.26	213
61.300	128.3944	55.9000	176	−	−
61.820	82.1964	7.6000	365	0.40	358
62.260	122.5447	63.5000	893	0.56	812
62.180	111.2951	50.0000	109	−	−
62.440	42.5981	−18.2000	5440	0.31	5758
62.700	42.5981	−17.8000	20690	0.35	20872
62.970	42.5981	−16.6000	9325	0.48	9620
63.140	30.4487	−19.7000	1090	0.30	1124
G33.980−00.019					
58.886	0.0000	0.0000	3782	0.33	4057
59.501	5.1225	0.1130	434	0.30	454
60.292	−50.1990	−23.9650	315	0.45	290

Table 6. continued.

V_{LSR} (km s^{-1})	ΔRA (mas)	ΔDec. (mas)	S_p (mJy beam^{-1})	*FWHM* (km s^{-1})	S_{amp} (mJy beam^{-1})
60.555	−29.6685	1.7760	254	0.29	258
61.258	−49.1925	−16.8830	784	0.37	797
61.609	30.1755	−5.5850	515	0.60	469
62.312	30.5595	−3.2980	276	0.40	248
64.157	16.2345	−27.9140	497	0.50	471
65.387	−32.4450	−40.9110	236	0.25	237
G34.751−00.093					
50.627	28.8631	−27.8740	224	0.59	215
51.769	−10.8418	−3.5670	718	0.46	702
52.736	0.0000	0.0000	1954	0.68	1817
53.175	−3.5980	−0.9420	1763	0.44	1845
G35.793−00.175					
60.060	−2.4000	−0.8600	889	0.27	952
60.680	0.0000	0.0000	9702	0.62	9616
61.300	1.9500	0.8100	6338	0.48	6327
61.820	3.0000	1.2100	5960	0.75	5927
62.350	4.3500	2.2100	1225	0.60	1347
G36.115+00.552					
70.395	−1072.0323	421.7720	10779	0.38	9795
70.834	−1075.7487	431.4520	254	0.33	261
71.186	−5.1454	0.8900	1066	0.40	1113
71.449	−1068.0478	420.0420	617	0.35	637
71.801	−1062.5353	420.6660	2921	0.28	2869
71.977	−24.9857	−12.5080	1386	0.29	1398
72.416	−1064.1711	421.8460	2973	0.63	2681
72.504	−1168.7980	300.8850	506	−	−
72.855	−1063.7741	421.0850	11194	0.35	11100
73.031	0.0000	0.0000	11744	0.49	11978
73.119	−39.3480	−27.3450	1431	0.58	1613
73.821	−1163.3500	155.9080	1134	0.19	1149
74.173	−48.5034	−43.3810	2845	0.39	3600
74.436	−43.6441	−45.4110	6641	0.54	5863
75.139	−9.8909	12.9190	371	0.35	357
75.579	−46.4093	−46.6400	316	0.36	302
75.754	7.3175	14.7340	431	0.28	431
76.106	0.1992	16.2260	3900	0.27	4007
81.289	−1122.9459	420.7460	1619	0.78	1373
81.553	−1100.4663	436.9820	447	0.77	386
81.816	−1103.1221	438.3080	513	0.27	515
81.904	−1116.3250	407.0410	1010	0.31	1103
82.168	−1113.5523	420.1690	5062	0.32	5183
83.925	−1116.4418	417.6580	1652	0.66	1816
G36.705+00.096					
52.560	1.3392	1.1530	348	0.33	353
53.087	0.0000	0.0000	7576	0.31	7608
53.790	−0.9167	−0.1560	2413	0.48	2470
54.405	−1.8934	−1.2010	4629	0.65	4404
54.844	−2.0102	−9.9610	1309	0.43	1343
55.108	−1.5579	−3.2250	420	−	−
62.137	−14.1016	52.0590	1974	0.45	1969
63.015	−0.3940	45.6080	153	0.47	154
G37.030−00.039					
78.585	0.0000	0.0000	691	0.47	656
78.761	−0.4374	0.2050	224	−	−

Table 6. continued.

| V_{LSR} (km s^{-1})	ΔRA (mas)	ΔDec. (mas)	S_p (mJy beam^{-1})	*FWHM* (km s^{-1})	S_{amp} (mJy beam^{-1})
G37.598+00.425					
82.802	91.6302	−11.1510	251	−	−
85.789	0.0000	0.0000	3911	0.43	3826
85.438	−0.3322	−0.8860	891	0.33	902
86.931	26.0379	12.9580	2407	0.32	2482
87.195	25.4768	13.1770	465	−	−
87.283	39.3823	6.436	2543	0.45	2661
88.600	63.5139	4.0650	395	−	−
88.688	66.2298	−7.5300	202	−	−
G38.038−00.300					
55.656	0.0000	0.0000	2168	0.34	1996
57.062	6.2921	−15.5470	507	−	−
57.413	9.3731	−16.4000	1046	0.38	980
58.204	13.9385	−1.8140	1434	0.25	1444
59.522	20.8441	−15.0610	215	−	−
59.522	19.9328	12.8000	224	−	−
59.609	19.0545	−3.8880	281	−	−
G38.203−00.067					
79.640	0.0000	0.0000	828	0.28	707
80.518	−54.8141	20.5190	169	−	−
80.606	11.2600	13.4970	157	0.38	160
83.856	−101.8398	154.2200	173	−	−
83.944	−35.3736	29.9400	152	−	−
83.944	−35.2315	44.9650	195	−	−
84.208	−33.8743	31.6240	198	−	−
G39.100+00.491					
14.630	−5.7037	−38.5700	222	−	−
14.630	−7.8346	−11.4310	453	0.28	446
15.772	13.3126	−22.0650	314	−	−
15.860	115.0769	103.8770	623	−	−
15.860	116.6086	75.8880	545	−	−
15.860	13.3112	−22.0040	769	−	−
15.245	0.0000	0.0000	2068	0.37	1803
15.684	−5.1254	−5.8070	1140	0.62	1158
15.948	−4.9192	−7.1320	1042	0.23	1108
17.617	6.6630	−8.1800	696	0.32	654
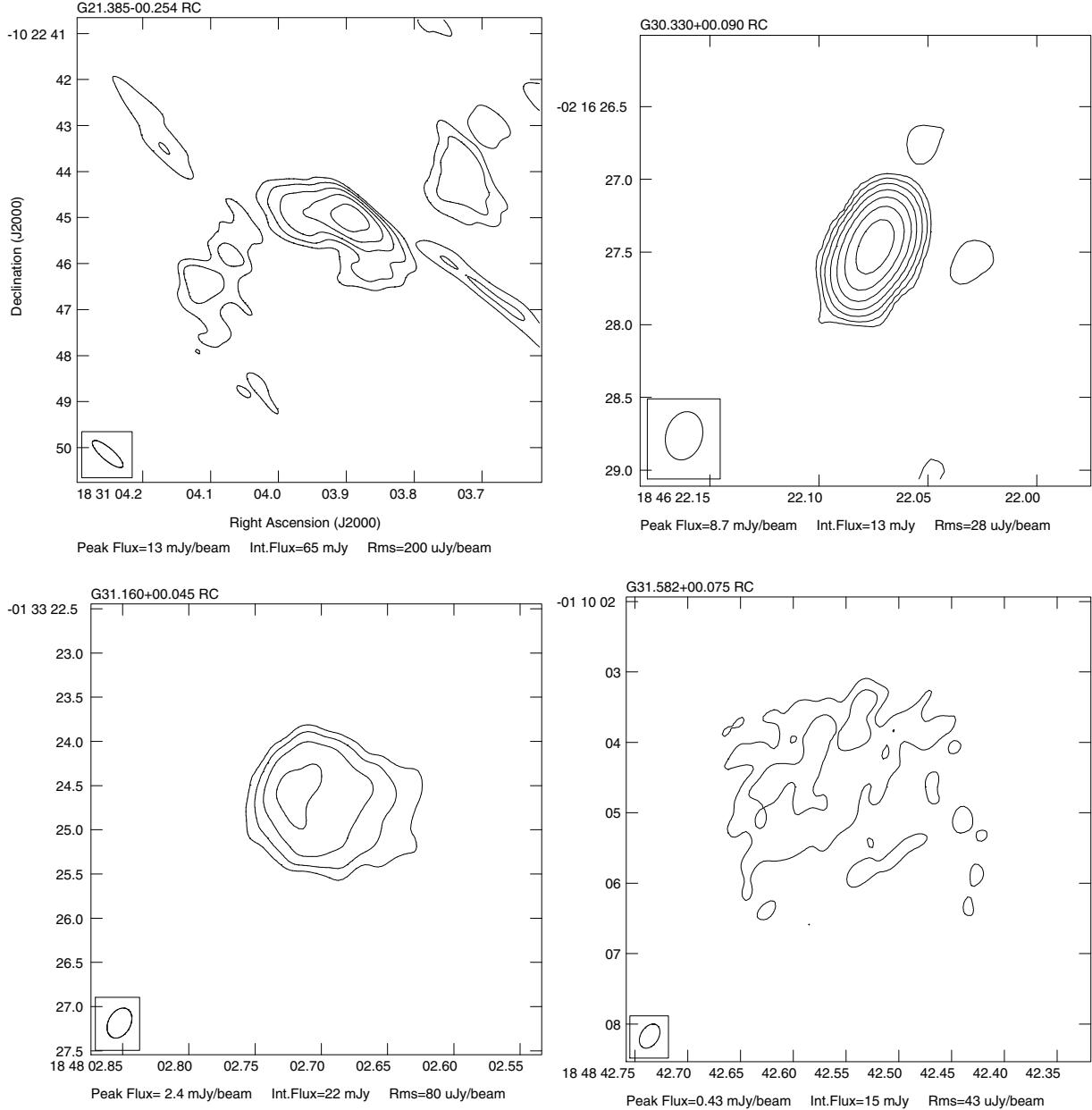
Fig. 3. The 8.4 GHz continuum emission detected using VLA on 2007 August 18. The names of radio continuum sources (RC) are the Galactic coordinates of peak fluxes. The peak and integrated fluxes as well as the levels of rms ($1\sigma_{rms}$) are given under each map and the beamsizes are presented at the left down corners. Contours trace the levels of $3\sigma_{rms} \times (1, 2, 4, 8, 16, 32, 64, ...)$.
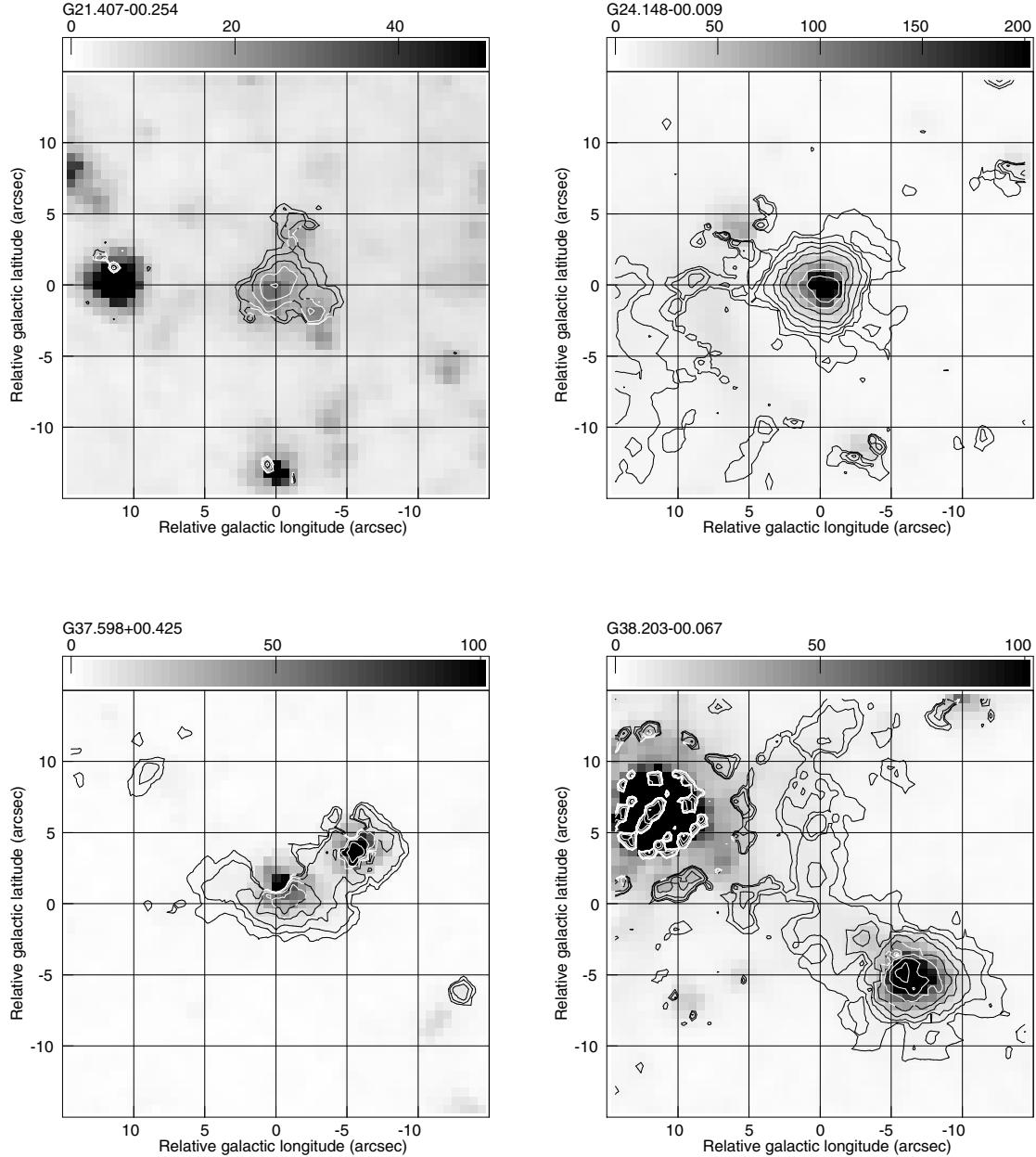
Fig. 6. *Spitzer* IRAC 4.5 μm (grey) and 4.5 μm−3.6 μm (contour) images centered on selected methanol sources (at coordinates taken from Table 5). The grey scale in MJy sr⁻¹ is indicated in the horizontal bar and contour levels are 1 MJy sr⁻¹× (1, 2, 4, 8, 16, 32, 64, 128). The methanol maser **G21.407−00.254** coincides exactly with the brightest pixel in the 4.5 μm−3.6 μm image, at the map origin, which is offset from the 4.5 μm peak. There are at least two other nearby MIR sources with 4.5 μm emission excesses. Note the absence of further sources with extended 4.5 μm−3.6 μm emission excess in this 30″ × 30″ field. The maser source **G24.148−00.009** coincides with the peaks of emission both at 4.5 μm and for the 4.5 μm−3.6 μm excess. The maser **G37.598+00.425** is offset from the brightest 4.5 μm emission. Note the highly asymmetric morphology of the extended 4.5 μm−3.6 μm excess emission and the coincidence of the maser emission with a maximum of this excess. In the case of **G38.203−00.067**, the maser emission does not coincide with either of the two brightest sources but is close (∼1″.7) to a weak bump of 4.5 μm−3.6 μm excess located in a very extended arc (∼25″) of diffuse 4.5 μm emission. Further inspection of IRAC images at 5.8 μm suggests that this bump could be a weak MIR object.